Ferric iron evolution during crystallization of the Earth and Mars

Laura Schaefer[1], Kaveh Pahlevan[2], Linda T. Elkins-Tanton[3]

[1] Department of Earth and Planetary Sciences, Stanford University
[2]Carl Sagan Center, SETI Institute, Mountain View, CA
[3]School of Earth and Space Exploration, Arizona State University,

Corresponding author: Laura Schaefer (lkschaef@stanford.edu)

Key Points:

- We model mineral/melt partitioning during magma ocean crystallization using new Fe^{3+} partition coefficients for lower mantle minerals.
- We calculate oxygen fugacity (fO_2) of outgassing at the surface for Earth and Mars magma oceans and match to constraints from planetary D/H.
- For Earth, only models using the Armstrong EOS match constraints, whereas Mars must start Fe^{3+}-depleted to match constraints.

Abstract

Magma ocean crystallization models that track fO_2 evolution can reproduce the D/H ratios of both the Earth and Mars without the need for exogenous processes. Fractional crystallization leads to compositional evolution of the bulk oxide components. Metal-saturated magma oceans have long been thought to contain negligible ferric iron oxide ($Fe^{3+}O_{1.5}$), but recent work suggests they may contain near-present-day Fe^{3+} concentrations of planetary mantles. We model the fractional crystallization of Earth and Mars, including Fe^{2+} and Fe^{3+} as separate components. We use two independent equations of state (Deng, Armstrong EOS) to calculate Fe^{3+} partition coefficients for lower mantle minerals and compare results of fractional crystallization for different magma ocean configurations for both Earth and Mars. We calculate the oxygen fugacity (fO_2) at the surface as the systems evolve and compare them to constraints on the fO_2 of the last magma ocean atmosphere from D/H ratios. For Earth, we find that Fe^{3+} must behave incompatibly in the lower mantle to match the D/H constraint for whole mantle models, but shallow magma ocean models also provide reasonable matches to the constraints. For Mars, both EOSs produce near identical results but cannot match the D/H constraints on last fO_2 unless the magma ocean begins with less than 50% of the predicted Fe^{3+}. This model shows that Fe^{3+} partitioning has a measurable effect on magma ocean atmosphere redox state, which is not a static quantity but evolves throughout the magma ocean's lifetime. We highlight the need for additional experimental constraints on ferric iron partitioning.

Plain Language Summary

During the formation of planets like Earth and Mars, many undergo a stage in which their rocky mantles are almost fully molten, called a magma ocean. The crystallization of different minerals as the magma ocean cools leads to changes in the composition of the melt. The melt maintains contact with the atmosphere throughout this stage, so changes in the melt's composition, especially the availability of oxygen, can lead to changes in the atmosphere's composition. In this paper, we use a model that looks at how the melt's composition changes, with a special focus on how different types (or species) of iron (Fe^{2+}, Fe^{3+}) behave as minerals form. We use two different models called equations of state (EOS) of how these iron species behave at high pressures and compare how the melt's composition changes when we use each of them. For Earth, only one of the EOS models produces results that agree with information that we have about the composition of the last atmosphere in contact with the magma ocean. For Mars, both models produce similar results, but neither is successful in recreating the last atmosphere unless the melt starts with much less of the Fe^{3+} species than previously predicted.

1. Introduction

The oxidation state of Earth's present day upper mantle is close to the quartz-fayalite-magnetite (QFM) buffer (Canil & O'Neill 1996; Frost & McCammon 2008), which results in oxidized volcanic gases such as H_2O and CO_2. Measurements of redox proxies going back to at least 3900 Ma (Delano 2001), and possibly as far back as 4.3 Ga (Trail et al. 2011), are consistent with present day values, indicating little secular change in mantle oxidation state through time, although recent measurements suggest a slightly lower mantle oxidation state during the early Archean of ~QFM-0.5/1 (Aulbach & Stagno 2016, Nicklas et al. 2019). However, models of core formation suggest that the Earth's mantle would have been two log units below the iron-wüstite buffer (~IW-2) at the end of planet formation (Rubie et al. 2015, Badro et al. 2015). As first suggested by Hirschmann (2012), recent measurements of ferric (Fe^{3+}) iron in silicate melts and first principles calculations indicate that high pressure conditions may stabilize ferric iron over ferrous iron (Armstrong et al., 2019; Zhang et al., 2017, Deng et al. 2020, Kuwahara et al. 2023), unlike earlier lower pressure data (Kress & Carmichael 1991; O'Neill et al. 2006). Fe-bearing silicates equilibrated at high pressure then have non-negligible ferric iron contents, even at reducing conditions. This suggests that once metal segregates during core formation, the oxygen fugacity of a well-mixed mantle at low pressures – often characterized by its Fe^{+3}/Fe^{+2} – would suddenly increase. Hirschmann (2022) recalibrated a silicate melt equation of state and calculated the ferric iron contents of silicate melts under core-formation conditions for Earth and Mars and found Fe^{3+}/Fe_T = 0.04 – 0.10 and 0.026 – 0.038, respectively, consistent with the present day mantles of the two planets.

Chemical partitioning models of magma ocean evolution have also previously shown that fractional crystallization will tend to increase the FeO abundance in the magma ocean during soldification (Elkins-Tanton et al., 2003, 2005). This results in a denser, iron-rich upper mantle, which may cause a massive early mantle overturn event (Boukaré et al. 2018; Elkins-Tanton et al. 2003). Ferric iron is moderately incompatible during both partial melting and fractional crystallization (Canil & O'Neill 1996; Cottrell & Kelley 2011; Sorbadere et al. 2018) in the upper mantle and may therefore fractionate from ferrous iron during fractional crystallization of the magma ocean, as first suggested by McCanta et al. (2009). Most previous fractional crystallization models did not include ferric iron because it was thought to be present at vanishingly small amounts for oxygen fugacities below IW. Fractionation of ferric and ferrous iron during magma ocean solidification would produce both vertical and temporal variations in redox state, which may influence mantle mineralogy as well as early outgassed atmospheric compositions.

In this paper, we seek to determine the effect that ferric iron partitioning could have on the oxygen fugacity of the last magma ocean atmospheres of Earth and Mars. Pahlevan et al. (2019, 2022) determine the oxygen fugacity of the last atmosphere equilibrated with a magma ocean by determining the maximum amount of D/H fractionation that could have occurred for Earth and Mars, using constraints on initial D/H of early hydrogen reservoirs. These models assume that all hydrogen that escapes is carried to the upper atmosphere in the form of H_2, and no hydrogen is stripped from water vapor during the steam atmosphere stage. Then the relative abundances of H_2 and H_2O in the last magma ocean atmosphere constrain the oxygen fugacity through the reaction:

$$H_2 + ½O_2 = H_2O \quad (1)$$

Assuming a chondritic source of early water on Earth, Pahlevan et al. (2019) find that only a small amount of hydrogen escape is allowed, which requires the oxygen fugacity of the last magma ocean atmosphere for Earth to be greater than IW + 1. Under these conditions, the abundance of H_2 is much lower than the abundance of H_2O in the gas phase equilibrated with the magma ocean. In contrast, there appears to be evidence for moderate to high escape of hydrogen from early Mars, and Pahlevan et al. (2022) find that the D/H ratio would be consistent with a last magma ocean atmosphere less than IW – 1. These constraints therefore provide a lower limit on oxygen fugacity for Earth but an upper limit for the last magma ocean atmosphere of Mars.

In this paper, we present models for ferric iron partitioning in a crystallizing magma ocean on Earth and Mars, considering both batch and fractional crystallization scenarios. Our model follows the evolution of the ferric iron as it partitions between mantle minerals and magma ocean liquid. To do this, we must first determine ferric iron partition coefficients for all the crystallizing minerals. Whereas measurements of ferric iron partition coefficients are available for many of the upper mantle minerals (Mallmann & O'Neill 2009, Davis & Cottrell 2021, Rudra & Hirschmann 2022), most of the lower mantle minerals have no such measurements. In this paper, we therefore use the best available mineral constraints in conjuction with a silicate melt model for the variation of Fe^{3+}/Fe^{2+} with oxygen fugacity in order to estimate the ferric iron partition coefficients. Two silicate melt equations of state (EOS) extend up to high enough pressure to use for these calculations (Armstrong et al. 2019, Deng et al. 2020). We find that these two EOSs yield opposite partitioning behavior (compatible vs. incompatible) for several of the lower mantle minerals, including bridgmanite. Our partitioning model therefore provides a test of the two EOSs to determine which model is most consistent with the D/H constraints for Earth and Mars.

This paper is organized as follows. We first discuss the model below and describe the ferric iron partition coefficients for the abundant mantle minerals (**Section 2**) using the two EOS parameterizations for ferric iron oxide (Armstrong et al. 2019, Deng et al. 2020). We then discuss what magma ocean conditions the D/H constraints of Pahlevan et al. (2019, 2022) may correspond to. We then show results for the fO_2 evolution at the surface for different initial ferric iron abundances and different crystallization scenarios (**Section 3**) for both planets to determine which model parameters best match the D/H constraints.

2. Magma ocean model

2.1 Fractional Crystallization: phases and proportions

In this paper, we modify the magma ocean fractional crystallization model of Elkins-Tanton (2008). The magma ocean crystallizes from a given depth (or pressure) upwards, following a specified mineralization sequence determined by mineral phase stability along the mantle solidus, with slightly different mineral proportions for Earth and Mars (Elkins-Tanton 2008, Table 2). We do not explicitly model the planetary thermal evolution timescales or volatile evolution here, focusing instead on the detailed mineral/melt chemical evolution. We update the Elkins-Tanton fractional crystallization model by modifying the internal structure calculation and including ferric/ferrous iron partitioning between the silicate liquid and crystallizing phases. We

also explore the uncertainties in the ferric iron partition coefficients using Monte Carlo simulations. We discuss these updates in detail below.

2.2 Internal structure

We specify the core mass fraction of the planet and then the internal structure of the planet is calculated for a liquid silicate mantle and isolated Fe core by solving the equations of internal structure with spherical symmetry and hydrostatic equilibrium:

$$\frac{dm(r)}{dr} = 4\pi r^2 \rho(r) \quad (2)$$

$$\frac{dP(r)}{dr} = \frac{-Gm(r)\rho(r)}{r^2} \quad (3)$$

As the planetary mantle solidifies, the density of the minerals in each solid layer is determined and the radius of solidification is calculated, beginning from the core-mantle boundary. The crystallization occurs in layers of 1 wt% of the mantle's mass. The depth of the magma ocean is determined for the new magma ocean composition by determining the density of the silicate liquid with depth. We compute the internal structure evolution for each of the magma ocean scenarios (see **Section 2.3**) once, to determine the evolution of the radius of solidification, then we use this calculated structure for each of the Monte Carlo simulations with different ferric iron partition coefficients. Using this procedure, the density of the layers that are strongly ferric iron-enriched may be slightly underestimated.

2.3 Whole Mantle vs. Shallow Magma Ocean Models

In our models, we test different magma ocean configurations for both Earth and Mars (see **Figure 1**), with either different initial depths of melting or a switch between crystallization style from batch (or equilibrium) to fractional crystallization. Purely fractional crystallization produces larger degrees of fractionation than batch crystallization, but the switch from batch to fractional crystallization depends on crystal size within the magma ocean (Solomatov 2015), with both mechanisms possible under the convective conditions of Earth's magma ocean. Xie et al. (2020) use new measurements of silicate liquid viscosities to calculate crystal fractions and find that fractional crystallization likely started when the base of Earth's magma ocean was ~1000 km depth, with formation of a bridgmanite-rich layer at the top of the lower mantle during batch crystallization. In the absence of good constraints on the Martian magma ocean, we will adopt identical scenarios for both planets. We test whole mantle magma ocean models in which batch crystallization switches to fractional crystallization at 500 km and 1000 km, as shown in **Figure 1(*left*),** compared to a fully fractional crystallization model. We also compare these results to shallow magma ocean models, also starting at 500 or 1000 km, in which we assume that the lower mantle does not melt and the starting compositions are the Bulk Silicate planet compositions given in **Table 1**. The differences in results between whole mantle vs. shallow magma oceans is driven entirely by the bulk composition at the initiation of fractional crystallization.

For the whole mantle models, we adopt a simplified model of batch crystallization, in which we compute bulk partition coefficients for each of the melt oxide phases via:

$$\overline{D} = \sum_i X_i D_i \quad (4)$$

where X_i is the mass fraction of mineral phase *i* in the solid, D_i is the partition coefficient between mineral *i* and the melt and $\bar{D}$ is the bulk partition coefficient between solid and liquid. We then use the batch crystallization equation to calculate the composition of the liquid following crystallization of some mass fraction of the mantle.

$$\frac{C_{liq}}{C_{liq}^0} = \frac{1}{F(1-\bar{D})+\bar{D}} = \frac{1}{F+\bar{D}(1-F)} \quad (5)$$

where F is the degree of melting, C_{liq} is the mass fraction of an oxide in the melt after crystallization, C_{liq}^0 is the initial mass fraction of the oxide in the magma ocean. The conditions for batch crystallization for each scenario are given in **Table 2**, including the pressure and temperature at the base of the magma ocean layer (top of solid layer), the mass fraction of the magma ocean relative to the total mantle, and the mineral mass fractions within the crystallized layer, normalized to 1. We use these mineral fractions in equation 5 for calculating bulk partition coefficients for each model. We adopt the same starting pressure and temperature conditions for the shallow magma ocean models.

In **Table S1**, we summarize the partition coefficients (D_i) for each of the melt oxide components (SiO_2, MgO, FeO, CaO, Al_2O_3) that we use in the batch crystallization model. Note that we do not specifically calculate mineral phase compositions or apply stoichiometric corrections as done during the fractional crystallization stage. We modify the exchange coefficients (e.g, $K_D^{Fe/Mg} = D_{FeO}/D_{MgO}$) for the fractional crystallization stage to ensure consistency with the D_i used in the calculation of the bulk partition coefficients (eqn 5). We summarize our new K_D values compared to the Elkins-Tanton (2008) model in **Table S2**. Most values are in relatively close agreement, and we find little change in the overall model behavior when using either set of values.

To take into account the uncertainties on the partition coefficients, we performed Monte Carlo simulations using 10^5 randomized draws of oxide partition coefficients, assuming uncorrelated normal distributions, to perform the batch crystallization calculations. These simulations produced mean oxide abundances that were reproducible within 0.01 wt%, which we use as the starting compositions for the fractional crystallization models. We report the mean values for each batch scenario in **Table 1**, along with the Bulk Silicate Earth (BSE) (McDonough 2003) and Bulk Silicate Mars (BSM) (Taylor 2013) compositions, which are also used as starting conditions for the shallow magma ocean models.

2.4 Pressure of last equilibration

To relate the oxygen fugacity predicted by our fractional crystallization models to the D/H constraints of Pahlevan et al. (2019, 2022), we must determine the conditions under which the magma ocean and the atmosphere begin to evolve separately. Magma ocean thermal evolution models suggest that the mantle evolves from a fully molten system to a partially molten "mush" system, at which point a thick lid (> a few km) can form (Solomatov 2007, Lebrun et al. 2012, Monteux et al. 2020). The lid inhibits direct magma ocean-atmosphere exchange, with subsequent transfer of volatiles from the interior to the atmosphere requiring physical advection

of material through the lid. This is often called the rheological transition. Some portion of the upper mantle remains molten at this stage, with additional volatiles trapped within the melt layer (Elkins-Tanton 2008, Hier-Majumder & Hirschmann 2017, Miyazaki & Korenaga 2022). We characterize the separation of the atmosphere and remaining magma ocean by the pressure at the base of the partially molten layer when the thick lid forms, which we refer to as the *basal pressure of last equilibration* (BPLE). We show an example thermal profile that illustrates the intersection of solidus and magma ocean adiabat that determines the BPLE in Figure S4. Although our fractional crystallization models continue to lower pressures than the BPLE, we search for models which produce the allowed oxygen fugacity within the bounds of the BPLE that we calculate below.

We use a 1D magma ocean thermal evolution model (Schaefer et al. 2016, Lebrun et al. 2013) to constrain the BPLE for both Earth and Mars. Note that this model is a physical simulation that is separate from the chemical model of fractional crystallization that we discuss throughout the rest of this paper. The thermal evolution model calculates the evolution of mantle and surface temperatures along with volatile evolution within the coupled mantle-atmosphere system. We find that the BPLE is not sensitive to the volatile content or any parameters that determine the timing of solidification. Instead, we find that the BPLE depends most sensitively on the assumed solidus and liquidus curves, and especially the temperature difference between the solidus and liquidus (T_{liquidus}-$T_{\text{solidus,}}$ called liquidus offset hereafter) within the upper mantle layers, which determines melt fraction (φ= ($T_{\text{mantle}} - T_{\text{solidus}}$)/($T_{\text{liquidus}}$-$T_{\text{solidus}}$)) and dictates the evolution of the rheological front. We find that if the liquidus offset is reduced, the BPLE drops to lower pressures.

A conservative assumption of a dry peridotite solidus and liquidus (Pierru et al. 2022) for Earth yields BPLE of 15.3 GPa. Pierru et al. (2022) find a liquidus offset of ~300 K in the upper mantle, which increases to ~600 K at the core-mantle boundary. We find similar BPLE values using Pierru et al (2022)'s solidus temperature with a constant liquidus offset of 300 K. However, the presence of volatiles such as water and CO_2 in the liquid will lower solidus and liquidus temperatures (Katz et al. 2003, Medard & Grove 2008). If we reduce both the solidus and liquidus temperatures equally by 200 and 400 K, we find BPLE for Earth of 14.6 and 14.0 GPa, respectively, a relatively small effect. If volatile effects do not equally reduce the solidus and liquidus temperatures, these results may vary more greatly, with higher (lower) BPLE values if the solidus-liquidus gap increases (decreases). An additional effect to consider is that fractional crystallization enriches the liquid in incompatible elements, which can produce an equal or greater decrease in the solidus temperatures compared to volatile-rich models (Elkins-Tanton 2008). Elkins-Tanton (2008) determined solidus temperatures for Earth and Mars by calculating melting points for their fractionally crystallizing systems using the MELTs model, incorporating both the incompatible element and volatile effects. We use their reported solidus temperatures with liquidus offsets ranging from 300 to 600 K and find BPLE from 6 – 10 GPa. Note also that we assume that the liquidus offset is constant with pressure, which is likely an oversimplification but provides reasonable upper and lower bounds.

The solidus temperature of Mars is different from the peridotite solidus of the Earth due to higher FeO contents. Liquidus temperatures are not well-determined for Mars, but based on work by Longhi et al. (1992), we estimate a solidus-liquidus offset of between 300 – 400 K. Duncan et al. (2018) measured solidus temperatures for Mars-analog compositions. Using their solidus plus

liquidus offsets of 300 – 400 K, we find BPLE of 2.8 – 3.8 GPa for Mars. This range is much lower than for the Earth due to the effect of the lower gravity of Mars on the temperature structure with pressure. We again find minimal differences if both solidus and liquidus are equally reduced by impurities. Elkins-Tanton (2008) also determined the solidus for a fractionally crystallizing Mars. Using their solidus with 300 – 400 K liquidus offsets, we find BPLE of 1.7 -2.5 GPa.

Based on these results, we adopt a range of 6 – 15 GPa for the BPLE for Earth, and 1.7 – 3.8 GPa for Mars. Miyazaki & Korenaga (2022) find a slightly lower but similar pressure of ~5 GPa for the base of the partially molten layer when the surface becomes solid for an Earth-mass planet. We emphasize that further investigation of the factors that control the pressure of last equilibration for magma ocean atmospheres, as well as the timing of separation of atmosphere and interior will be necessary to further our understanding of the early atmospheres of rocky planets.

2.5 Ferric iron partitioning

Our chemical models of fractional crystallization allow the oxygen fugacity of the magma ocean to evolve as a result of changes in the ferric to ferrous iron ratio (Fe^{3+}/Fe^{2+}) in the silicate melt. This ratio evolves as a result of differences in the partitioning behavior of the two iron oxide species. To study this, we modify the model of Elkins-Tanton (2008) by adding ferric iron partitioning between the silicate minerals and melt. The ferric iron partition coefficients used for each mineral along with estimated uncertainties are given in **Table 3**. Models have shown that the bulk FeO content of the melt phase will increase as the magma ocean crystallizes due to the incompatibility of Fe relative to Mg in silicate minerals (Boukaré et al. 2018; Elkins-Tanton et al. 2003). Fe/Mg partition coefficients have been updated from previous models (see **Section 2.3**) and are assumed to represent Fe^{2+} only. Ferric iron also behaves as a moderately incompatible element in most mineral/melt systems (Canil and O'Neill, 1996). Bulk partition coefficients for ferric oxide in peridotite/melt systems under upper mantle conditions are typically found to be between 0.1 – 0.3 (Canil & O'Neill 1996; Cottrell & Kelley 2011; Sorbadere et al. 2018). Cottrell and Kelley (2011) calculated a bulk Fe_2O_3 partition coefficient of 0.22 for fertile mantle composed of 55% olivine, 25% orthopyroxene, 18% clinopyroxene and 2% spinel using the partition coefficients of Mallmann and O'Neill (2009). The comparable value of the bulk mantle/melt partition coefficient for FeO using the same mineralogy is 0.85, indicating that ferrous iron behaves more compatibly than ferric iron. Therefore, our expectation is that the Fe^{3+}/Fe^{2+} ratio of the magma ocean should increase as the magma ocean crystallizes, although this depends in detail on the crystallizing phases and their proportions. In particular, the ferric iron abundance and partitioning behavior in the lower mantle minerals are largely unknown, but they have been shown to have a high capacity to hold ferric iron under current mantle conditions in mineral physics experiments.

For most of the minerals in our model, we assume a constant mineral/melt partition coefficient derived from experiments. It is likely that ferric iron partition coefficients depend on other factors, including pressure, temperature, oxygen fugacity, melt fraction, electronic spin state and/or bulk composition. However, there is insufficient experimental data to robustly constrain these dependencies for any major mantle phase beyond the upper mantle. We consider the ferric iron partition coefficients presented here to be the best current achievable estimate, but we

emphasize the need for additional experimental measurements in order to better constrain the evolution of magma ocean redox state.

In **Section 3**, we will explore how the uncertainty in the ferric iron partition coefficients may alter the results of the calculations and the implications for the evolution of the earliest atmospheres of Earth and Mars. Below, we briefly discuss the partition coefficients for the phases included in this model, and the typical Fe^{3+} abundance observed in mantle samples where available. Additional literature review of ferric iron partition coefficients is available in **Text S1**.

2.5.1 Upper mantle assemblage (ol, opx, cpx, sp)

We halt crystallization of the magma ocean model at 2 GPa, as accumulated compositional fractionation may alter low pressure crystallization sequences, and mass balance becomes difficult to achieve with our prescribed mineralogy. We therefore do not include plagioclase in the following discussion, which only crystallizes at pressures less than 2 GPa.

2.5.1.1 Olivine (ol) Fe^{3+} is highly incompatible in olivine, and typically has abundances below reporting standards in most upper mantle olivines. Many models of partitioning during partial melting of the upper mantle assume that $D_{Fe^{3+}}^{ol/melt} = 0$ (e.g. Canil et al. 1994, Rudra & Hirschmann 2022). Mallmann & O'Neill (2009) find a non-zero but very low partition coefficient of 0.0626 ± 0.0102 for Fe^{3+} into olivine. We adopt a partition coefficient of 0 for olivine, but calculations using the partition coefficient of Mallmann & O'Neill (2009) do not produce significantly different results.

2.5.1.2 Spinel (sp) Spinel is a major host phase for ferric iron in the upper mantle. Although it is not an abundant mineral, ferric iron is very compatible in spinels. In lherzolite peridotites in the present day upper mantle, spinel has $Fe^{3+}/\Sigma Fe$ of 15-34% (Woodland et al. 2006). Davis & Cottrell (2021) conducted peridotite partial melting experiments at 1.5 GPa and over a range of fO_2. Using their data along with corrected data from Sorbadere et al. (2018), Davis & Cottrell (2021) find that $D_{Fe^{3+}}^{sp/melt}$ increases with spinel Fe_2O_3 concentration, independent of fO_2, and decreases with temperature. We adopt their corrected $D_{Fe^{3+}}^{sp/melt}$ equation:

$$lnD_{Fe_2O_3}^{sp/melt} = a\frac{10{,}000}{T} + b + c\ ln\left(C_{Fe_2O_3}^{sp}(\text{wt\%})\right) \quad (6)$$

where a = 0.87 ± 0.07, b = -4.6 ± 0.4, and c = 0.24 ± 0.02.

2.5.1.3 Clinopyroxene (cpx)- and Orthopyroxene (opx) Ferric iron is more compatible in clinopyroxene than orthopyroxene, making it an important host phase in the upper mantle. In modern day lherzolite peridotites, opx and cpx have $Fe^{3+}/\Sigma Fe$ = 2 – 9% and 3 – 32%, respectively (Woodland et al. 2006). Rudra & Hirschmann (2022) used experiments on an andesite composition liquid to measure the Fe^{3+} partition coefficient for cpx at 1 – 2.5 GPa. They found that it depends on both the Al_2O_3 and Fe_2O_3 concentrations in the clinopyroxene, although the fit including Fe_2O_3 gives only marginal improvement over fitting by Al_2O_3 alone, which we prefer for simplicity. This relationship is given by the equation:

$$D_{Fe^{3+}}^{cpx/melt} = (0.165 \pm 0.047)C_{Al_2O_3}^{cpx}(\text{wt\%}) + (-0.297 \pm 0.108) \quad (7)$$

However, this equation gives negative values for the partition coefficient when Al_2O_3 is below 1.8 wt%, which is within the range of natural abundances for cpx in garnet peridotites (Woodland 2009). Therefore, we refit this relationship using logarithmic values for both *D* and Al_2O_3 concentration. We include the three cpx/melt values from Davis and Cottrell (2021), which are at higher Al_2O_3 concentration, and derive:

$$\ln D_{Fe^{3+}}^{cpx/melt} = (1.997 \pm 0.640) \ln C_{Al_2O_3}^{cpx}(\text{wt\%}) + (-3.987 \pm 0.965) \quad (8)$$

We find an $r^2 = 0.6027$, compared with $r^2 = 0.575$ for the equation given in Rudra & Hirschmann (2022) (see **Fig. S1**).Our model finds Al_2O_3 concentrations of 0.5 – 1.5 wt% in clinopyroxene, with slightly wider ranges in whole mantle models (batch + fractional crystallization) versus shallow mantle models (fractional crystallization only). High pressure clinopyroxenes are typically Mg-rich, becoming more Ca-rich as crystallization progresses. Because of the strong dependence on Al_2O_3 abundance, the cpx partition coefficients are much lower (~0.05) than those determined by Mallmann & O'Neill (2009) of 0.45, which leads to slighlty stronger fractionation of ferric iron in the upper mantle. This effect is further propagated by linking the clinopyroxene partition coefficient to those of orthopyroxene and garnet, as discussed below.

The ferric iron partition coefficient of orthopyroxene is poorly constrained by experimental data, especially regarding compositional dependencies. We follow Rudra & Hirschmann (2022) in using the relationship:

$$D_{Fe^{3+}}^{opx/melt} = D_{Fe^{3+}}^{opx/cpx} \times D_{Fe^{3+}}^{cpx/melt} \quad (9)$$

We fit data on ferric iron concentration in opx and cpx in peridotites to a log-normal distribution, which gives $D_{Fe^{3+}}^{opx/cpx} = 0.70^{+1.56}_{-0.64}$ (Woodland et al. 2006, Canil & O'Neill 1996, Malaspina et al. 2012, Nimis et al. 2015, Luth & Canil 1993) (see **Fig. S2**). We note that this is close to, but somewhat lower than the values of 0.80 (Rudra & Hirschmann 2022, fit to normal distribution) and 0.81 (Davis and Cottrell 2021, constrained by 3 experimental data points). Typical values of $D_{Fe^{3+}}^{opx/melt}$ in our models range from 0.02 – 0.05.

2.5.2 Garnet (gt)

Garnet in upper mantle peridotites typically has $Fe^{3+}/\Sigma Fe = 2 – 7\%$ (Canil & O'Neill 1996, Malaspina et al. 2012, Nimis et al. 2015). As with other high pressure phases, little to no information is available on partitioning of ferric iron between silicate melt and garnet, although data is available on partitioning of ferric iron between garnet and pyroxene phases in natural samples (Canil & O'Neill 1996, Woodland et al. 2006, Woodland 2009, Nimis et al. 2015, Aulbach et al. 2022). We therefore again adopt the parameterization of Rudra & Hirschmann (2022), using the relationship:

$$D_{Fe^{3+}}^{gt/melt} = D_{Fe^{3+}}^{gt/cpx} \times D_{Fe^{3+}}^{cpx/melt} \quad (10)$$

We fit a log-normal distribution to data from natural peridotites, which yields $D_{Fe^{3+}}^{gt/cpx} = 0.68^{+1.96}_{-0.51}$ (Woodland 2009, Canil & O'Neill 1996, Malaspina et al. 2012, and Nimis et al. 2015) (see **Fig.**

S3). Typical values of $D_{Fe^{3+}}^{gt/melt}$ in our models range from 0.02 – 0.05. We note that this model does not capture the temperature dependence of gt/cpx partition coefficients noted by others (Canil and O'Neill 1996, Woodland 2009, Purwin et al. 2013). The garnet/cpx partition coefficient determined here is biased to sub-solidus temperatures. Because the garnet/cpx partition coefficient increases with temperature, using a constant value may underestimate the ferric iron partition coefficient that would be appropriate for a magma ocean system. We discuss the effect of uncertainties on the garnet partition coefficient further in **Section 4.1**.

2.5.3 Majorite (maj), Wadsleyite (wad), Ringwoodite (ring)

Ferric iron is more compatible in the high-pressure phases wadsleyite and ringwoodite than in the lower pressure polymorph olivine and becomes increasingly more compatible in the majoritic form of garnet at high pressures. However, there are few studies that report measured ferric iron content of these minerals along with co-existing minerals like pyroxene or garnets and none with melts. However, minimum ferric iron abundances in the minerals have been measured at metal saturation. O'Neill et al. (1993) found that the minimum $Fe^{3+}/\Sigma Fe$ of majorite, wadsleyite, and ringwoodite coexisting with metallic iron was 0.07, 0.03 and 0.04, respectively. For magma ocean conditions at or below IW, we expect similar ferric iron contents in these minerals. We use the silicate melt model of Hirschmann (2022) for a melt that would hypothetically co-exist with the minerals at these conditions in order to estimate the ferric iron partition coefficient. We use both the Deng and Armstrong EOS for ferric iron oxide ($FeO_{1.5}$). We report our calculated average values in **Table 3**, with details about the calculation provided in **Text S2** and **Table S1**.

2.5.4 Bridgmanite (bg)

Boujibar et al. (2016) report Fe^{3+}/Fe_T measurements of bridgmanite specimens under partial melting conditions at 25 GPa and IW – 2, with values ranging from 14 – 25%. They also report degree of melting and the bulk oxide abundances of both minerals and the quenched melt phase. We use the measured fO_2 and melt phase abundances to calculate the Fe^{3+}/Fe_T ratio in the silicate melt using the model of Hirschmann (2022) and both the Deng and Armstrong EOS for ferric iron oxide ($FeO_{1.5}$). Additional details are given in the **Text S3** and **Table S2**. We find an average value of $D_{Fe^{3+}}^{bg/melt}$ of 2.07 ± 0.50 with the Deng EOS and 0.17 ± 0.03 with the Armstrong EOS. The two equations of state predict radically different partitioning behavior of ferric iron in bridgmanite. More recently, Kuwahara & Nakada (2023) report ferric iron partition coefficients between silicate melt and bridgmanite at 23-27 GPa, with values of $D_{Fe^{3+}}^{bg/melt} = 0.43 - 0.51$. These experiments were at fO_2 conditions slighlty below the Re-ReO_2 buffer, with calculated values of IW+1.0 to +1.5 (note that we calculate slightly higher fO_2 than reported in the paper, assuming pure Re metal foil, as alloy compositions were not reported). These experiments, as well as work by Kuwahara et al. (2023), suggest closer agreement with the Armstrong EOS, although Kuwahara et al. adopt different values for the first pressure derivative of the bulk modulus κ' of both FeO and $FeO_{1.5}$ of 4 and 1.4, compared to 8 and 1.3 from Armstrong et al. . In our model below, we prefer our calculated partition coefficients for bridgmanite rather than the more recent measurements by Kuwahara et al. for three reasons: 1) the Boujibar et al. (2016) experiments occur at oxygen fugacity conditions more consistent with predicted magma ocean conditions post-core-formation (e.g. IW-2, Rubie et al. 2015), 2) they allow us to explore a more extreme range of partitioning behaviors in the lower mantle, and 3) to conduct a consistent test of a single EOS's predictions for ferric iron partitioning behavior. We

explore how the outcomes of our models change when using the partition coefficient of Kuwahara et al. in **Section 4.1**. There is a clear need for more partitioning experiments at a wider range of experimental conditions in order to better constrain deep mantle behavior.

2.5.5 Magnesiowüstite (mw)

Magnesiowüstite (or ferropericlase) contains a relatively small amount of ferric iron, ranging from ~0 to 0.1 times the ferrous iron abundance (McCammon et al. 2004a) when in equilibrium with metallic iron. At higher oxygen fugacities, periclase can incorporate more significant amounts of ferric iron. Otsuka et al. (2013) show that the ferric iron abundance in periclase depends strongly on composition (Fe#), oxygen fugacity, and pressure. They find that ferric iron abundances can be large for Fe# > ~ 0.2 at relatively high oxygen fugacities. However, ferric iron abundances are likely negligible (< 1%) for all reasonable Fe#s at pressures greater than ~ 24GPa. Measurements of natural ferropericlase inclusions in diamonds from the lower mantle find $Fe^{3+}/\Sigma Fe \lesssim 7\%$ (Kaminsky et al. 2015; McCammon et al. 1997, 2004b), consistent with the experimental results. For our calculations, we therefore neglect ferric iron in magnesiowüstite under the assumption that the lower mantle will begin crystallizing at a relatively low (<IW) fO_2.

2.5.6 Testing uncertainties

We report estimated uncertainties for the ferric iron partition coefficients in **Table 3**. To explore how these uncertainties would affect the redox evolution of the crystallizing magma ocean, we perform Monte Carlo simulations with 1000 random draws from normal distributions (log-normal for opx/cpx and gt/cpx) for each of the ferric iron partition coefficients. For clinopyroxene and spinel, we draw for each of the fit coefficients from equations (6) and (8). We assume all uncertainties are uncorrelated. We found that 100 draws was sufficient to produce stable mean values for Fe^{3+}/Fe_T and fO_2 but that the ranges of these calculated values were substantially smaller than when using 1000 simulations. In order to more accurately estimate the uncertainty on the calculated fO_2, we used the larger number of simulations. Simulations beyond 1000 did not substantially change means or increase calculated ranges but did substantially increase computation time.

2.6 Initial Fe^{3+} abundance

Hirschmann (2022) calculated ferric iron contents of magma oceans for Earth and Mars at core-forming conditions, using different pressure-temperature-fO_2 from literature models of trace element behavior during core-formation. He found ranges of $Fe^{3+}/Fe_T = 0.034 – 0.10$ for Earth and 0.026 – 0.038 for Mars, depending on mantle FeO_T abundance. We use these as our starting range of ferric iron abundance in our magma ocean models. Hirschmann (2022) modified his calculated ferric iron abundance due to Cr^{2+} oxidation during sub-solidus reactions with Fe^{3+} in the upper mantle. We neglect this effect here as we are largely focused on the liquid silicate behavior. We start with nominal abundances of $Fe^{3+}/Fe_T = 0.10$ for Earth and 0.02 for Mars. More recently, Kuwahara et al. (2023) experimentally found a $Fe^{3+}/Fe_T = 0.2 – 0.5$ for peridotite under metal-saturated conditions at pressures of 23 – 28 GPa. While these numbers are challenging to explain from a mantle redox evolution perspective (Hirschmann 2023), they are consistent with a modified Armstrong et al. (2019) EOS for $FeO_{1.5}$. We will therefore explore a range of initial Fe^{3+}/Fe_T up to 0.20.

2.7 Interstitial Liquids

Previous magma ocean models have noted that in the crystallization of magma chambers, some liquid is often trapped by the crystals that settle to the bottom of the magma chamber. Elkins-Tanton et al. (2005) adopted an interstitial liquid volume fraction in each solid layer of 1%. Recent models by Hier-Majumder & Hirschmann (2017) & Miyazaki & Korenga (2022) looking at the two-phase dynamics of magma ocean crystallization have suggested that the trapped liquid fraction may be much higher, especially in the upper mantle, and increase as the rate of solidification increases. Hier-Majumder & Hirschmann (2017) find trapped liquid fractions of 20-30 vol% in the upper mantle. This has implications for trapped volatile fraction but will also modify the results of our redox-partitioning model explored here. We find the effect to be minor in comparison to uncertainties on the ferric iron partition coefficients. We use a nominal value of 20% in our fractional crystallization models but discuss results with as little as 1%. Effects of interstitial fluid on compositional fractionation are minimal for pressures higher than 5 GPa.

3 Results

In the following section, we discuss the oxygen fugacity evolution of the magma oceans of Earth and Mars, with a focus on matching the constraints for the D/H ratios of the last magma ocean atmospheres at the BPLE. We show results for different initial Fe^{3+} abundances and consider the different magma ocean depths and crystallization scenarios discussed in **Section 2.6** and **Figure 1**. The evolution of the oxide abundances within the solid and liquid phases largely matches the results of previous work (Elkins-Tanton et al. 2003, 2005, Elkins-Tanton 2008), with increasing concentration of incompatible oxides such as FeO, CaO, and Al_2O_3 and decreasing concentrations of compatible oxides including MgO and SiO_2 in the late-stage liquid. We provide a brief description of these results in **Supplemental Text S4** but focus here on the new results related to Fe^{3+} partitioning and oxygen fugacity.

3.1 Fe^{3+} Evolution of the Terrestrial Magma Ocean

The Deng and Armstrong EOSs produce opposite ferric iron partitioning behavior in the lower mantle, with the Deng EOS yielding compatible behavior ($D_{Fe^{3+}}^{min/melt} > 1$) and the Armstrong EOS yielding incompatible behavior ($D_{Fe^{3+}}^{min/melt} < 1$) (see **Table 3**). For the Deng EOS, ferric iron concentrations therefore decrease during crystallization of the lower mantle and transition zone, whereas ferric iron concentrations increase for the Armstrong EOS. Within the upper mantle, ferric iron partition coefficients are identical and Fe^{3+} concentrations generally increase due to bulk partition coefficients being much less than 1.

The oxygen fugacity of a silicate melt can be calculated using the ratio of Fe^{3+} to Fe^{2+} (Kress & Carmichael, 1991, O'Neill et al. 2006, Jayasuriya et al. 2004, Zhang et al. 2017, Armstrong et al. 2019, Sossi et al. 2020, Deng et al., 2020). Here we use the recently recalibrated equation of Hirschmann (2022) to calculate the oxygen fugacity at the surface of the magma ocean, which is relevant for the outgassed atmosphere. This equation depends on the pressure, temperature and oxide abundances of the silicate liquid as follows:

$$\log\left(\frac{X_{FeO_{1.5}}}{X_{FeO}}\right) = a\log f_{O_2} + b + \frac{c}{T} - \frac{\Delta C_p}{R\ln 10}\left[1 - \frac{T_0}{T} - \ln\left(\frac{T}{T_0}\right)\right] - \frac{\int_{P_0}^{P}\Delta V dP}{RT\ln 10} + \frac{1}{T}\left[Y_1X_{SiO_2} + Y_2X_{TiO_2} + Y_3X_{MgO} + Y_4X_{CaO} + Y_5X_{NaO_{0.5}} + Y_6X_{KO_{0.5}} + Y_7X_{PO_{2.5}} + Y_8X_{SiO_2}X_{AlO_{1.5}} + Y_9X_{SiO_2}X_{MgO}\right] \quad (11)$$

where parameter values are given in **Table 4**, T is temperature in K, P is pressure in GPa, and X_i are mole fractions of the oxides in the silicate melt. We calculate the temperature at the surface of the magma ocean by assuming a one-phase magma ocean adiabatic profile anchored by the solidus temperature at the base of the magma ocean. We assume a pressure of 1 bar at the surface, so that the ΔVdP term is negligible. Models suggest that magma oceans may have atmospheres of 100 – 1000 bars (e.g. Hamano et al. 2013, Lebrun et al. 2013), but this produces a very minor pressure effect that we neglect here. We also utilize the evolving oxide mole fractions determined with the fractional crystallization model (see **Figure S8**) in equation (11). This calculation assumes that the composition of the silicate liquid remains homogeneous throughout the liquid layer due to rapid convection and therefore that the relative concentrations of Fe^{3+} and Fe^{2+} and the other oxides are the same at both the surface and the base of the magma ocean. Note that we prefer the relationship between Fe^{3+}/Fe^{2+} and fO_2 from Hirschmann (2022) rather than Sossi et al. (2020) because of the dependence on the oxide mole fractions in the silicate melt, which deviate from the peridotite composition measured by Sossi et al. after fractional crystallization.

Figure 2 shows the evolution of the oxygen fugacity of outgassing for the whole mantle magma ocean models, with either fully fractional crystallization (*right*, 'whole Earth') or a switch from batch to fractional crystallization occurring at 500 (*left*) or 1000 km (*middle*). The base of the magma ocean evolves from right to left in these figures, with time from start of crystallization following in the same direction, although note that we do not specifically model the timing of solidification. For these calculations, we use a nominal initial $Fe^{3+}/Fe_T = 0.10$. This value is the upper limit of Fe^{3+}/Fe_T determined for core-formation conditions by Hirschmann (2022). In **Figure 2**, we plot all 1000 draws of different ferric iron partition coefficient values in grey and the average of the 1000 simulations in black. The calculations shown in the top row use partition coefficients for the lower mantle and transition zone calculated with the Deng EOS, whereas the bottom row uses those derived with the Armstrong EOS. The pink horizontal shaded region shows the allowed fO_2 of the last magma ocean atmosphere from D/H constraints (Pahlevan et al. 2019) and the gray vertical shaded region shows our constraints for the BPLEBPLE from **Section 2.4**; the overlap between pink and gray areas represent valid solutions.

The oxygen fugacity evolution closely follows the ferric iron content of the magma ocean. Therefore the Deng EOS models produce a decreasing fO_2 as pressures drop from 120 GPa to 18 GPa (**Fig. 2, *right* and *middle*)** due to crystallization of bridgmanite, majorite, ringwoodite and wadsleyite, whereas the Armstrong EOS produces increasing fO_2 across the same region. The Armstrong EOS produces a smaller spread in solutions because of the smaller absolute value and therefore smaller uncertainty on the bridgmanite partition coefficient compared to the Deng EOS (note that we treat both uncertainties as a normal distribution, truncated at zero). For both EOS models, the 500 km magma ocean shows increasing fO_2 as the magma ocean crystallizes up to pressures of ~5 GPa and a relatively narrow range of possible solutions, but note that the Armstrong EOS model starts at much higher fO_2 because of the incompatible behavior of Fe^{3+} during the batch crystallization stage. In contrast, the fO_2 of both the 1000 km and whole Earth models using Deng EOS partition coefficients initially decrease before increasing at pressures less than ~20 GPa. This is due to the compatible behavior of ferric iron in the transition zone and lower mantle minerals, unlike the upper mantle. At pressures lower than 5 GPa, Fe^{3+} in the liquid and fO_2 of outgassing decreases due to a) increase in $D_{Fe^{3+}}^{cpx/melt}$ because of increasing Al_2O_3

contents in the cpx phase, and b) the eventual crystallization of spinel, which has a large $D_{Fe^{3+}}^{sp/melt}$ value.

Only 7 of the 3000 realizations (all for the whole Earth fractional model) of Deng EOS models shown in **Fig. 2(*right*)** produce results that agree with the combined D/H and BPLE bounds. In contrast, all 3000 realizations of the Armstrong EOS models produce valid solutions. The successful Deng EOS models have an average bridgmanite partition coefficient of 1.00 in comparison to the average for all of the whole Earth Deng EOS models of 1.99. Taken at face value, the D/H constraints suggest that the Armstrong EOS produces more realistic ferric iron partition coefficients, and therefore that ferric iron behaved incompatibly throughout the entire magma ocean.

However, it is possible that the initial ferric iron content of the magma ocean was either higher or lower than our nominal value and that the Deng EOS could produce results consistent with D/H with different initial conditions. **Figure 3** shows only the mean oxygen fugacities for the three different whole mantle configurations with different starting Fe^{3+}/Fe_T from 0.04 up to 0.20. For the Deng EOS models, initial Fe^{3+}/Fe_T of 0.04 and 0.14 do not produce valid solutions to the D/H constraints. For the initial $Fe^{3+}/Fe_T = 0.20$, we find that 993, 47, and 249 realizations out of 1000 match the 500 km, 1000 km and whole Earth models, respectively (see **Table S5**). In contrast, effectively all realizations of all Armstrong EOS models match the D/H constraints within the BPLE bounds. The Armstrong EOS model only fails if Fe^{3+}/Fe_T is less than 0.04. However, we note that for $Fe^{3+}/Fe_T > 0.10$, the Armstrong EOS models predict fO_2 greater than the present day upper mantle, which are likely too high to be valid. Recent experimental work by Kuwahara et al. (2023) suggests that initial mantle Fe^{3+}/Fe_T was 0.2-0.50 and favors the Armstrong EOS over the Deng EOS, although with modified κ' for both FeO and $FeO_{1.5}$. We find these conclusions contradictory with the extreme redox evolution of the models using the Armstrong EOS developed here.

To find whether there are any configurations under which the Deng EOS predicts valid solutions, we additionally consider shallow magma oceans, by beginning the 500 km and 1000 km models with a BSE composition (see **Fig.1 (*right*)**). Shallow magma oceans may be generated by smaller impactors in which only a portion of the mantle is melted. Alternatively, some models suggest that a magma ocean may solidify from the middle of the mantle, with a basal magma ocean crystallizing much more slowly than the upper mantle portion of the magma ocean (Labrosse et al. 2007). Our shallow magma ocean models could then be interpreted as simulating the upper mantle portion of such a layered crystallization model. By using BSE as the starting composition, we assume that the mantle is homogenized prior to settling of crystals to the starting depth (either 500 or 1000 km), followed by upward fractional crystallization. We plot the averages of these realizations as dashed lines in **Figure 3**. These realizations are much more successful at matching the D/H constraint for the Deng EOS because the BSE has a higher starting Fe^{3+}/Fe_T than the batch crystallization models. For the 500 km partial magma ocean, 0, 989 and 1000 realizations match for initial $Fe^{3+}/Fe_T = 0.04$, 0.10, and 0.14. For the 1000 km magma ocean, 0, 620 and 976 realizations are successful for the same initial Fe^{3+}/Fe_T. Bulk partition coefficients are similar (see **Figure S5**) between the whole mantle and shallow magma ocean models, with outcomes differing due to the differences in ferric iron content of the magma ocean when fractional crystallization begins.

We also run simulations with different amounts of interstitial liquid, as discussed in **Section 2.7**. Our nominal simulations use 20% interstitial fluid. We neglect the compositional evolution of the interstitial fluid as it crystallizes in situ. Smaller amounts of interstitial fluid generate slightly more compositional fractionation, with differences becoming significant at pressures less than 5 GPa. These models produce steeper increases of Fe^{3+} in the liquid and therefore higher oxygen fugacities for outgassing. However, since the BPLEBPLE for Earth is at pressures higher than 5 GPa, interstitial fluid abundance does not affect our conclusions regarding the oxygen fugacity at the time that the atmosphere and magma ocean begin to evolve separately.

3.2 Fe^{3+} Evolution of a Martian Magma Ocean

Our nominal model for Mars used initial $Fe^{3+}/Fe_T = 0.02$, slightly lower than the range of values calculated for core formation conditions by Hirschmann (2022) of 0.026 – 0.038 (see **Figure S6**). The D/H constraint for Mars (Pahlevan et al. 2022) is a maximum fO_2 of IW-1 for the last magma ocean atmosphere. All of the whole mantle magma ocean models produce monotonically increasing values for Fe^{3+}/Fe_T and fO_2 of outgassing with decreasing pressure, due to incompatible Fe^{3+} behavior throughout most of the Martian mantle. Because there is only a small portion of the Martian mantle containing high pressure phases, the Deng and Armstrong EOS models produce nearly identical results within ~0.5 log units of fO_2 of each other, unlike the Earth models, although the Deng models are modestly more successful, especially for the whole mantle fractional crystallization model. For calculations using our nominal ferric iron abundance, most models produce oxygen fugacities of IW to IW+1 at 2 GPa. Only 265, 89, and 875 out of 1000 simulations are successful for the three Deng EOS models, but 0, 2, and 171 for the Armstrong models. The successful simulations have bulk ferric iron partition coefficients roughly an order of magnitude higher than the mean in the 2.5-15 GPa region, where olivine, orthopyroxene, clinopyroxene and garnet all form. Reducing the initial ferric iron content of the planet produced more successful results for both EOS models.

In **Figure 4**, we show simulations for a lower initial $Fe^{3+}/Fe_T = 0.01$ for the three whole mantle magma ocean models, which provides a better fit to the constraints. This initial ferric iron content is substantially lower than predicted values but produces 100% successful outcomes for all three whole mantle batch crystallization models for both EOSs. Successful models have oxygen fugacities lower than IW-1 somewhere within the predicted BPLEBPLE range, although not necessarily at the lowest pressure. In **Figure 5**, we compare mean values for 1000 simulations for the whole mantle and shallow magma ocean models with different initial Fe^{3+}/Fe_T.

The shallow magma oceans, which start from the Bulk Silicate Mars (BSM) composition (see dashed lines for 500 and 1000 km models), diverge more strongly for the 500 km models at low pressure, and more so for the Armstrong EOS than the Deng EOS. As for the Earth, these models simulate either shallower magma oceans, or ones that produce a neutrally buoyant cumulate pile at midmantle depth that isolates the upper mantle from the lower mantle. For the 1000 km models, evolution is nearly identical to the whole mantle crystallization case, with the $Fe^{3+}/Fe_T = 0.01$ model producing 100% successful simulations, whereas with $Fe^{3+}/Fe_T = 0.02$, there are only ~1% successful simulations for both EOSs. In comparison, the 0.02 model for the 500 km partial magma ocean produces 100% successful simulations for both EOSs. Changes in interstitial fluid

produce larger increases in oxygen fugacity as pressure decreases, so there are fewer successful realizations for each magma ocean model. However, mean values for $Fe^{3+}/Fe_T = 0.01$ with both 20% and 1% interstitial fluid are successful for all three magma ocean depths.

Based on the D/H constraints within the BPLE, the initial ferric iron content of Mars may have been lower than calculated from core-formation conditions. This could be achievable through less efficient equilibration between the mantle and core or continuous accretion of metal-bearing building blocks rather than a single-stage core formation scenario that sets the magma ocean redox state. Alternatively, a shallow, 500 km magma ocean with higher initial Fe^{3+}/Fe_T would also match the observed D/H constraints. Another possible solution is that our calculated BPLE is too low and the separation between atmosphere and magma ocean occurs at higher pressures, where oxygen fugacities are lower. This would be possible if the liquidus offset was smaller than the 300-400 K that we assumed, or if the solidus were steeper than the Elkins-Tanton (2008) model.

Bulk ferric iron partition coefficients are shown in **Figure S7**. The ferric iron partition coefficient does not change significantly for different initial Fe^{3+}/Fe_T, and bulk partition coefficients are generally the same for all of the whole mantle (batch + fractional crystallization) models for a given mineralogical layer. Partition coefficients are greater than 1 at pressures above 15 Gpa for the Deng EOS models, where wadsleyite, ringwoodite and majorite form, but slightly below 1 in this pressure region for the Armstrong EOS models. In the upper mantle, the 2.5-15 Gpa layer contains olivine, orthopyroxene, clinopyroxene and garnet. Partition coefficients are largely determined by Al_2O_3 content in clinopyroxenes, which is low. A spike in the bulk partition coefficient at low pressure occurs where spinel begins to form. Ferric iron is compatible in spinel, but the bulk partition coefficient remains less than 1 because of the relatively small phase proportion of spinel.

4. Discussion

4.1 Ferric iron partition coefficient uncertainties

Ferric iron mineral-melt partition coefficients for several critical mineral phases remain mostly unmeasured. We have estimated those quantities here to the extent possible, but a high degree of uncertainty remains. In particular, garnet plays a key role in the redox budget of the upper mantle, but there have been no direct measurements of ferric iron mineral-melt partition coefficients. There is only one direct measurement of the ferric iron partition coefficient (Kuwahara and Nakada 2023) of bridgmanite and no direct measurements of ferric iron partition coefficients for any of the other lower mantle minerals (majoritic garnet, wadsleyite, ringwoodite). In addition, the pressure, temperature and compositional dependencies of ferric iron partition coefficients would be valuable to improve our understanding of the redox evolution of the Earth's mantle.

Figures 2 & 4 show the effect of the current estimated uncertainties of the current ferric iron partition coefficient estimates on the oxygen fugacity calculations. Both the 1000 km and whole mantle models for the Deng EOS have much larger uncertainties on the fO_2 evolution than for the 500 km model. This is because the uncertainties on the ferric iron partition coefficients of the lower mantle minerals allow both incompatible and compatible behaviors, which produce a

wider spread of behaviors. In contrast, ferric iron partition coefficients of the upper mantle are very small and absolute uncertainties are therefore also much smaller than the lower mantle, producing a narrower range of outcomes. However, this likely does not capture the full uncertainties of partitioning because we do not include the uncertainty of the major oxide partitioning, which effects cpx, and therefore opx and gt, partition coefficients.

The Armstrong EOS produces nearly compatible behavior for ringwoodite, wadsleyite, and majorite, whereas the Deng EOS predicts strongly compatible behavior for these minerals. The two EOS predict more contrasting behavior for bridgmanite (~2 vs. ~0.2), but the calculated uncertainty for the Armstrong EOS led us to only explore a narrow range of strongly incompatible states, as opposed to the moderately incompatible behavior shown by Kuwahara & Nakada (2023). To explore how our model results would be affected if these minerals (bg, ring, maj, wad, as well as gt) had ferric iron partition coefficients that produced different compatibility behavior, we run simulations of the whole Earth magma ocean with lower values of ferric iron partition coefficients (0.50 ± 0.50 for bg (based on Kuwahara & Nakada 2023), 0.50 ± 0.50 for ring and maj, 0.25±0.25 for wad) for all of the lower mantle minerals and a higher value for garnet (1.75 ± 0.75). We run each of these changes individually to determine which partition coefficient has the strongest effect on the fO_2 evolution (**Figure 6a**), otherwise using the Deng EOS ferric iron partition coefficients. We find minimal effects of changing the partition coefficients of ringwoodite, wadsleyite, majorite and garnet. However, bridgmanite has a very strong effect on the fO_2 evolution. Within the BPLE region, average fO_2 are 3 log units higher than the nominal model, approximately the same as the Armstrong EOS results, and match the D/H constraints on fO_2 very well. This effect is due to the very large volume fraction which bridgmanite occupies in the whole Earth model (~70 vol% of whole mantle), whereas all of the transition zone minerals combined occupy only ~8 vol%. Garnet has similarly low volume fraction (~1.5 vol%) and therefore has only a minor effect. Therefore this test confirms that the primary difference between the Deng and Armstrong EOS results is due to the radically different ferric iron partition coefficients these two EOS predict for bridgmanite.

We vary the same ferric iron partition coefficients for the whole Mars model, shown in **Fig. 6b**. We find a much smaller effect on the magma ocean oxygen fugacity for Mars. Increasing the garnet partition coefficient causes a drop in the final oxygen fugacity of ~0.5 log units, whereas decreasing all of the lower mantle mineral partition coefficients together increases the final oxygen fugacity ~0.5 log units. Garnet occupies ~6 vol% of the Martian mantle, whereas the combined lower mantle minerals (ringwoodite, majorite, wadsleyite) occupy ~ 21%. Note that variations for Mars are much smaller than for Earth because there is no bridgmanite present. Overall, we find that the largest improvements in the Earth and Mars models would come from more constraints on the ferric iron partition coefficient of bridgmanite and garnet under conditions appropriate to a magma ocean.

4.1.1 Bridgmanite

Since bridgmanite's mineral-melt partition coefficient has the largest effect on the Earth model outcomes, it is worth discussing in more detail. The abundance of ferric iron in bridgmanite under current mantle conditions has been shown to depend on Al content, oxygen fugacity, temperature, and total Fe content (Huang et al. 2021). In addition, ferric iron content seems to vary with depth in the modern mantle (Kurnosov et al. 2017, Mashino et al. 2020), likely due to

changes in substitution mechanisms at different pressures (Shim et al. 2017), which may be caused by changes in the spin state of Fe^{3+} on the B site (Lin et al. 2013). Shim et al. (2017) find that the Fe^{3+}/Fe_T of bridgmanite may drop to low values (~0.10) between 1,000 and 1,700 km, with higher values (>0.50) at both higher and lower pressures. Our nominal whole Earth model ($Fe^{3+}/Fe_T = 0.10$), which assumes both constant ferric iron partition coefficient as well as Fe/Mg exchange coefficient, produces bridgmanite with $FeO_T = 4 – 6$ wt% (Deng EOS) or 3-6% (Armstrong EOS) increasing at lower pressures, whereas $(Fe^{3+}/Fe_T)_{bg}$ decreases from ~0.40 at the core mantle boundary to ~0.10 at 22 GPa for the Deng EOS, but only changes from 0.05 – 0.06 for the Armstrong EOS. The variations with depth are due to the enrichment of the melt with FeO and relative depletion/enrichment of $FeO_{1.5}$. Although we can artificially impose a decrease in the ferric iron partition coefficient for the depths suggested by Shim et al. (2017), we find that doing so produces a minimal change in the oxygen fugacity evolution. For the Armstrong EOS, we find maximum values of $(Fe^{3+}/Fe_T)_{bg}$ of 0.11 when the initial bulk $(Fe^{3+}/Fe_T) = 0.20$. Achieving higher values of $(Fe^{3+}/Fe_T)_{bg}$ of 0.50 would require initial bulk (Fe^{3+}/Fe_T) up to or greater than 0.50, which would predict final outgassed atmospheres with fO_2 = IW+7 – IW+9, well above present day upper mantle oxidation state (QFM ~IW+4) and high enough that molecular O_2 gas would be significant in the outgassed atmosphere. We find this an implausible result, given evidence that the Archean mantle was 1 to 2 log units more reduced than the present day (Aulbach & Stagno 2016, Nicklas et al. 2019, Gao et al. 2022, Stagno & Aulbach 2021). However, note that the late accretion of small reduced planetesimals throughout the Hadean and late Archean may have delivered sufficient metal to reduce the upper mantle to the observed Archean values (Pahlevan et al. 2019, Kuwahara & Nakada 2023).

The thermodynamic model of Huang et al. (2021) shows that at a given pressure, Fe^{3+}/Fe_T in bridgmanite increases with decreasing temperature. Therefore, as the lower mantle cools below the solidus, Fe^{3+} should become more stabilized in bridgmanite, and additional disproportionation is likely to occur to increase the Fe^{3+}/Fe_T of the lower mantle. This is further supported by evidence that a metallic phase could be present within the modern day mantle (Frost et al. 2004, Rohrbach et al. 2007, Rohrbach & Schmidt 2011, Zhang et al. 2016). Therefore, we should not expect our magma ocean model to predict present-day Fe^{3+} abundances in bridgmanite. Pressure or temperature-dependence of the ferric iron partition coefficient or later thermochemical modification or mixing may account for the differences between our predictions for the magma ocean vs. present day mantle. However, a better understanding of how much disproportionation has occurred over the planet's lifetime is necessary to permit better modeling of the redox evolution during both the magma ocean stage and subsequent evolution.

4.2 Redox effects not included

In this paper, we have explored only the crystal-liquid chemistry of a dry, volatile-free magma ocean, and so these models are strictly only applicable to volatile-depleted planets. However, it is likely that the final magma oceans of both the Earth and Mars contained nearly their full complement of planetary volatiles. Recent experimental works have shown that all of the major volatile elements (H, C, N, S) can be highly soluble in core-forming alloy fluids under various conditions (Hirschmann 2016, Dalou et al. 2019, Grewal et al. 2019). Following the segregation of the core, volatiles within the magma ocean will partition between the atmosphere and silicate liquid based on their solubilities to form the earliest atmospheres (e.g. Elkins-Tanton 2008). Carbon and sulfur may exsolve as separate solid/liquid species, including carbides, sulfides,

graphite, and diamonds (Grewal et al. 2020, Gaillard et al. 2022). The compositions of secondary phases will depend strongly on the redox. Redox reactions between volatile elements and Fe-bearing species may also play a role in both the overall redox balance and the final composition of the system (Gaillard et al. 2014, 2022) as well as long term evolution (Hirschmann 2023). For instance, Genda & Ikoma (2008) and more recently Young et al. (2023) suggest that all of Earth's water could be produced by redox reactions between solar nebular H_2 gas with FeO-bearing silicate liquids within the magma ocean. Similar models have also been applied to exoplanets (Kite & Schaefer 2021, Schlichting & Young 2022). While these volatile-driven redox mechanisms are likely important for the overall redox evolution, incorporating them into the model presented here would require a more complete thermodynamic model for reactions between volatiles and iron-bearing species in both the melt and each mineral species throughout the full pressure range of the Earth's mantle, which is beyond the scope of this paper.

We note that additional redox evolution is likely to happen in the crystallizing mushy upper mantle layers, including post-solidus evolution due to Cr^{2+} oxidation by Fe^{3+} reduction (Hirschmann 2022), which we do not model here. Other redox sensitive elements such as Ti and V are also likely to play a role in the redox evolution as well, but are relatively low in abundance and are likely to produce more second-order effect. Given the large uncertainties in the behavior of ferric iron alone, the additional complexity of including these minor elements is not warranted at this time.

Sub-solidus reactions as well as crystallization of trapped interstitial melts are also likely to modify the Fe^{3+}/Fe_T of the mantle past the point where our models halt, so we do not expect our models to produce a direct match to the present day mantle. In addition, post-magma ocean mantle overturn and solid state convection will redistribute ferric and ferrous iron throughout the modern day mantle. Recent models suggest that, chondritic D/H values notwithstanding, solid state convection may initiate within the solidified cumulate layer below a liquid layer, even before full solidification, which may erase some of the density stratification generated by magma ocean crystallization (Maurice et al. 2017, Ballmer et al. 2017, Boukare et al. 2018, Morison et al. 2019, Bolrao et al. 2021, Sharp et al. 2013).

Because many of our models predict oxygen fugacities that are well below IW, many of our models may be metal-saturated, especially for low initial Fe^{3+}/Fe_T values for the Earth models. While the initial Fe^{3+}/Fe_T values are set by metal-silicate partitioning (Hirschmann 2022) under different conditions, removal of Fe^{3+} from the liquid by mineral/melt partitioning forces the liquid phase into below metal saturation. Therefore additional Fe^{3+} and metal production may occur during the magma ocean crystallization. We choose not to model this process here in the interest of minimizing the number of free parameters in the model, but in future work, we will explore how much additional disproportionation may occur as a result of crystallization.

4.4 Atmosphere evolution beyond the rheological transition

Using the thermal evolution model from **Section 2.4**, we examine the rate and timing of outgassing that occurs following the lid formation to estimate how quickly post-magma ocean outgassing will modify the last magma-ocean-equilibrated atmosphere. Unlike the BPLE, the timing of outgassing is sensitive to the absolute values of the solidus and liquidus temperatures, not just their offset. For dry solidus temperatures (Pierru et al. 2022), solid state outgassing for

the Earth can increase the atmospheric mass by 10% in 2 – 14 Myr, depending on initial volatile budget. However, if the solidus is depressed by 200 K, then it takes 200-300 Myr to see a similar increase in atmospheric mass. Bower et al. (2019) similarly find that outgassing pauses for ~100 Myr following solidification of the surface for an Earth-mass planet using a mixing-length thermal evolution model. The long pause before outgassing resumes suggests that the last magma ocean atmosphere remains unmodified by outgassing for a sufficient length of time for D/H fractionation to occur, such that the D/H constraint (Pahlevan et al. 2019) for Earth is a true probe of the oxygen fugacity of the magma ocean. We note that the Sun is most active and capable of driving atmospheric escape for the first 100 Myr after formation, so this lag in outgassing may distinctly separate a last magma ocean atmosphere from outgassing occurring in the mush mode. Recent work by Miyazaki & Korenaga (2022) suggests that upward melt transport via percolation may enhance early outgassing. However, Monteux et al. (2020) showed that the remaining melt layers may take 500 – 800 Myr to fully crystallize. We stress the need for additional dynamical magma ocean models to further assess the behavior of volatile transport during this time period.

For Mars, we find continued outgassing can increase the atmospheric mass by 10% within ~0.5 Myr when using the dry solidus (Duncan et al. 2018), but may take as much as 150-170 Myrs when the dry solidus is depressed by 200 K. Given the fast formation time of Mars (< 10 Myr, Dauphas & Pourmand 2011), solid-state outgassing may initiate well within the early active period of the Sun. Therefore, the lag in outgassing fluxes after surface solidification may not robustly separate the last magma ocean atmosphere from subsolidus outgassing, so it is possible that the D/H record for Mars may probe an atmosphere combined of both last magma ocean atmosphere and early sub-solidus outgassing.

5 Conclusions

In this paper, we show that it is possible to match the the D/H ratios of both the Earth and Mars through fractional crystallization of a magma ocean without the need for exogenous processes. We explore the redox evolution of magma oceans due to the different crystallization behaviors of ferric and ferrous iron.

We also constrain the pressure at the base of the magma ocean at the time of last atmosphere-mantle equilibration (BPLE). Magma ocean thermal evolution models predict a spread of pressures that depends sensitively on the gap between solidus and liquidus temperatures. Fractional crystallization and volatile trapping in melt will both act to lower solidus and liquidus temperatures, although it remains unclear if the effect on both is equal. More experimental data on residual liquid compositions, including both solidus and liquidus temperatures, are needed to better constrain the behavior of the late-stage magma ocean-atmosphere system, and subsequent outgassing. Further exploration of the dynamics of crystallization and melt sequestration during the late stage magma ocean is also needed to better understand what constitutes the last magma ocean atmosphere.

Hirschmann (2022) has calculated from first principles what the initial ferric iron content of Earth (Fe^{3+}/Fe_T = 0.034 – 0.10) and Mars (Fe^{3+}/Fe_T = 0.026 – 0.038) should be at the time of core formation using new data and equations of state for FeO and $FeO_{1.5}$. The range of ferric iron abundances span observed values for the present day. However, no whole mantle model for the

Earth with these ferric iron contents match the last magma ocean atmosphere oxygen fugacity, based on measurements of D/H ratios (Pahlevan et al. 2019) when using lower mantle ferric iron partition coefficients calculated with the Deng EOS. The best fitting model for the Earth with the Deng EOS requires shallow magma ocean conditions, starting from a Bulk Silicate Earth composition with initial Fe^{3+}/Fe_T above ~0.06. A partial magma ocean could be explained by either an impact smaller than the moon-forming impact, or by the formation of a buoyant layer of minerals at mid-mantle depths that leads to separate evolution of an upper and lower (basal) magma ocean. However, a likelier explanation for the Earth is that the Armstrong EOS provides a more accurate description of lower mantle ferric iron partitioning, which is strongly incompatible. This is consistent with new bridgmanite partition coefficient measurements by Kuwahara and Nakada (2023). We find that all of our tested Earth magma ocean scenarios with the Armstrong EOS except the lowest initial Fe^{3+}/Fe_T are consistent with the D/H constraints.

For Mars, best fit models have initial ferric iron abundances ~2.5x lower than predicted values, but partial magma oceans produce somewhat better matches to the D/H constraint. Because the minerals wadsleyite, ringwoodite, and majorite do not make up a significant portion of the Martian mantle, there is little difference between the Deng and Armstrong EOS models for Mars. If the magma ocean and atmosphere are separated when the magma ocean still has a greater depth than our predicted BPLE, then it would be possible to match the D/H constraint with larger initial ferric iron abundances more consistent with predictions.

We emphasize the need for more experimental data on ferric iron partition coefficients and melting temperatures of diverse compositions. Experimental synthesis of bridgmanite and transition zone minerals suggests that ferric iron could behave more compatibly in the lower mantle than the upper mantle, but unfortunately, there is little data on mineral/melt partition coefficients for lower mantle minerals and the two available equations of state for ferric iron oxide predict opposite partitioning behavior for these minerals. Some key upper mantle minerals (garnet) are likewise missing direct measurements of ferric iron partitioning with a co-existing melt. In particular, measurements of the ferric iron partition coefficients of bridgmanite and garnet will produce the biggest improvements in redox evolution models.

There remain many uncertainties in the redox evolution of magma oceans on rocky planets. We show that the most likely behavior for solar system bodies is an overall net increase in oxygen fugacity of outgassing, but this behavior does not necessarily hold true for all planets, depending on the bulk composition and minerals that form at different depths. Because we find that ferric iron must behave incompatibly in the lower mantle in order to match the Earth, we find that larger planets such as super-Earths, which have larger lower mantle volumes, will likely produce higher final oxygen fugacities than a smaller planet of the same initial composition. Therefore, on average, larger planets should produce more oxidized initial atmospheres than smaller planets.

Acknowledgments

LS and LTET acknowledge funding from the NASA Psyche mission and the NSF CSEDI program. KP acknowledges funding from the Keck foundation. We thank Fabrice Gaillard and an anonymous reviewer for helpful reviews on a previous version of this manuscript and Marc Hirschmann for helpful discussions.

Open Research

The magma ocean crystallization simulation code developed in this article is available at the Stanford Digital Repository (Schaefer, 2023a, https://doi.org/10.25740/yg376bh0915) along with all necessary input files to run the simulations shown in Figures 2-5. Matlab data files of all simulations are available in the archive.

The magma ocean thermal evolution model used in Section 2.7 and 4.1 is a modified version of the model described by Schaefer et al. (2016). The code used in this paper is archived at the Stanford Digital Repository (Schaefer, 2023b, https://doi.org/10.25740/rk050tc3031).

The literature data used to calculate ferric iron partition coefficients and bulk oxide partition coefficients are provided in the supplemental material as an .xlsx file.

References

Andrault, D., Bolfan-Casanova, N., Nigro, G. L., Bouhifd, M. A., Garbarino, G., & Mezouar, M. (2011). Solidus and liquidus profiles of chondritic mantle: Implication for melting of the Earth across its history. Earth and Planetary Science Letters, 304(1-2), 251-259. https://doi.org/10.1016/j.epsl.2011.02.006

Armstrong, K., Frost, D. J., McCammon, C. A., Rubie, D. C., & Boffa Ballaran, T. (2019). Deep magma ocean formation set the oxidation state of Earth's mantle. Science, 365(6456), 903-906. https://doi.org/10.1126/science.aax8376

Aulbach, Sonja, and Stagno, V. (2016) Evidence for a reducing Archean ambient mantle and its effects on the carbon cycle. Geology, 44, 751-754. https://doi.org/10.1130/G38070.1

Aulbach, S., Woodland, A. B., Stagno, V., Korsakov, A. V., Mikhailenko, D., & Golovin, A. (2022). Fe^{3+} Distribution and $Fe^{3+}/\Sigma Fe$-Oxygen Fugacity Variations in Kimberlite-Borne Eclogite Xenoliths, with Comments on Clinopyroxene-Garnet Oxy-Thermobarometry. Journal of Petrology, 63(8), egac076. https://doi.org/10.1093/petrology/egac076

Badro, J., Brodholt, J. P., Piet, H., Siebert, J., & Ryerson, F. J. (2015). Core formation and core composition from coupled geochemical and geophysical constraints. Proceedings of the National Academy of Sciences, 112(40), 12310-12314. https://doi.org/10.1073/pnas.1505672112

Ballmer, M. D., Lourenço, D. L., Hirose, K., Caracas, R., & Nomura, R. (2017). Reconciling magma-ocean crystallization models with the present-day structure of the Earth's mantle. Geochemistry, Geophysics, Geosystems, 18(7), 2785-2806. https://doi.org/10.1002/2017GC006917

Bertka, C. M., & Fei, Y. (1997). Mineralogy of the Martian interior up to core-mantle boundary pressures. Journal of Geophysical Research: Solid Earth, 102(B3), 5251-5264. https://doi.org/10.1029/96JB03270

Beyer, C., Myhill, R., Marquardt, K., & McCammon, C. A. (2021). A reversed redox gradient in Earth's mantle transition zone. Earth and Planetary Science Letters, 575, 117181. https://doi.org/10.1016/j.epsl.2021.117181

Bolrão, D. P., Ballmer, M. D., Morison, A., Rozel, A. B., Sanan, P., Labrosse, S., & Tackley, P. J. (2021). Timescales of chemical equilibrium between the convecting solid mantle and over-and underlying magma oceans. Solid Earth, 12(2), 421-437. https://doi.org/10.5194/se-12-421-2021

Boujibar, A., Bolfan-Casanova, N., Andrault, D., Bouhifd, M.A., Trcera, N., 2016. Incorporation of Fe^{2+} and Fe^{3+} in bridgmanite during magma ocean crystallization. Am. Mineral. 101, 1560–1570. https://doi.org/10.2138/am-2016-5561

Boukaré, C.-E., Parmentier, E.M., Parman, S.W., 2018. Timing of mantle overturn during magma ocean solidification. Earth Planet. Sci. Lett. 491, 216–225. https://doi.org/10.1016/j.epsl.2018.03.037

Bower, D. J., Kitzmann, D., Wolf, A. S., Sanan, P., Dorn, C., & Oza, A. V. (2019). Linking the evolution of terrestrial interiors and an early outgassed atmosphere to astrophysical observations. Astronomy & Astrophysics, 631, A103. https://doi.org/10.1051/0004-6361/201935710

Canil, D., O'Neill, H. S. C., Pearson, D. G., Rudnick, R. L., McDonough, W. F., & Carswell, D. A. (1994). Ferric iron in peridotites and mantle oxidation states. Earth and Planetary Science Letters, 123(1-3), 205-220. https://doi.org/10.1016/0012-821X(94)90268-2

Canil, D., O'Neill, H.S.C., 1996. Distribution of ferric iron in some upper mantle assemblages. J. Petrol. 37, 609–635. https://doi.org/10.1093/petrology/37.3.609

Chen, M., Goresy, A. E., Frost, D., & Gillet, P. (2004). Melting experiments of a chondritic meteorite between 16 and 25 GPa: Implication for Na/K fractionation in a primitive chondritic Earth's mantle. European Journal of Mineralogy, 16(2), 203-211. https://doi.org/10.1127/0935-1221/2004/0016-0203

Corgne, A., Liebske, C., Wood, B. J., Rubie, D. C., & Frost, D. J. (2005). Silicate perovskite-melt partitioning of trace elements and geochemical signature of a deep perovskitic reservoir. Geochimica et Cosmochimica Acta, 69(2), 485-496. https://doi.org/10.1016/j.gca.2004.06.041

Corgne, A., Armstrong, L. S., Keshav, S., Fei, Y., McDonough, W. F., Minarik, W. G., & Moreno, K. (2012). Trace element partitioning between majoritic garnet and silicate melt at 10–17 GPa: Implications for deep mantle processes. Lithos, 148, 128-141. https://doi.org/10.1016/j.lithos.2012.06.013

Corgne, A., & Wood, B. J. (2004). Trace element partitioning between majoritic garnet and silicate melt at 25 GPa. Physics of the Earth and Planetary Interiors, 143, 407-419. https://doi.org/10.1016/j.pepi.2003.08.012

Cottrell, E., Kelley, K.A., 2011. The oxidation state of Fe in MORB glasses and the oxygen fugacity of the upper mantle. Earth Planet. Sci. Lett. 305, 270–282. https://doi.org/10.1016/j.epsl.2011.03.014

Dalou, C., Koga, K. T., Hammouda, T., & Poitrasson, F. (2009). Trace element partitioning between carbonatitic melts and mantle transition zone minerals: Implications for the source of carbonatites. Geochimica et Cosmochimica Acta, 73(1), 239-255. https://doi.org/10.1016/j.gca.2008.09.020

Dalou, C., Hirschmann, M. M., Jacobsen, S. D., & Le Losq, C. (2019). Raman spectroscopy study of COHN speciation in reduced basaltic glasses: Implications for reduced planetary mantles. Geochimica et Cosmochimica Acta, 265, 32-47. https://doi.org/10.1073/pnas.1820719116

Dauphas, N., Pourmand, A. Hf–W–Th evidence for rapid growth of Mars and its status as a planetary embryo. Nature 473, 489–492 (2011). https://doi.org/10.1038/nature10077

Davis, F. A., & Cottrell, E. (2018). Experimental investigation of basalt and peridotite oxybarometers: Implications for spinel thermodynamic models and Fe3+ compatibility during generation of upper mantle melts. American Mineralogist: Journal of Earth and Planetary Materials, 103(7), 1056-1067. https://doi.org/10.2138/am-2018-6280

Davis, F. A., & Cottrell, E. (2021). Partitioning of Fe_2O_3 in peridotite partial melting experiments over a range of oxygen fugacities elucidates ferric iron systematics in mid-ocean ridge basalts and ferric iron content of the upper mantle. Contributions to Mineralogy and Petrology, 176(9), 67. https://doi.org/10.1007/s00410-021-01823-3

Delano, J.W., 2001. Redox history of the Earth's interior since ~3900 Ma: Implications for prebiotic molecules. Orig. Life Evol. Biosph. 31, 311–341. https://doi.org/10.1023/A:1011895600380

1057 Deng, J., Du, Z., Karki, B. B., Ghosh, D. B., & Lee, K. K. (2020). A magma ocean origin to
1058 divergent redox evolutions of rocky planetary bodies and early atmospheres. Nature
1059 communications, 11(1), 2007. https://doi.org/10.1038/s41467-020-15757-0

1060 Drake, M. J., McFarlane, E. A., Gasparik, T., & Rubie, D. C. (1993). MG-perovskite/silicate
1061 melt and majorite garnet/silicate melt partition coefficients in the SYSTEM CaO-MgO-SiO_2 at
1062 high temperatures and pressures. Journal of Geophysical Research: Planets, 98(E3), 5427-5431.
1063 https://doi.org/10.1029/92JE02290

1064 Draper, D. S., Xirouchakis, D., & Agee, C. B. (2003). Trace element partitioning between garnet
1065 and chondritic melt from 5 to 9 GPa: implications for the onset of the majorite transition in the
1066 martian mantle. Physics of the Earth and Planetary Interiors, 139(1-2), 149-169.
1067 https://doi.org/10.1016/S0031-9201(03)00150-X

1068 Duncan, M. S., Schmerr, N. C., Bertka, C. M., & Fei, Y. (2018). Extending the solidus for a
1069 model iron-rich Martian mantle composition to 25 GPa. Geophysical Research Letters, 45(19),
1070 10-211. https://doi.org/10.1029/2018GL078182

1071 Dwarzski, R. E., Draper, D. S., Shearer, C. K., & Agee, C. B. (2006). Experimental insights on
1072 crystal chemistry of high-Ti garnets from garnet-melt partitioning of rare-earth and high-field-
1073 strength elements. American Mineralogist, 91(10), 1536-1546.
1074 https://doi.org/10.2138/am.2006.2100

1075 Elkins-Tanton, L.T., 2008. Linked magma ocean solidification and atmospheric growth for Earth
1076 and Mars. Earth Planet. Sci. Lett. 271, 181–191. https://doi.org/10.1016/j.epsl.2008.03.062

1077 Elkins-Tanton, L.T., Parmentier, E.M., Hess, P.C., 2003. Magma ocean fractional crystallization
1078 and cumulate overturn in terrestrial planets: Implications for Mars. Meteorit. Planet. Sci. 38,
1079 1753–1771. https://doi.org/10.1111/j.1945-5100.2003.tb00013.x

1080 Elkins-Tanton, L. T., Hess, P. C., & Parmentier, E. M. (2005). Possible formation of ancient
1081 crust on Mars through magma ocean processes. *Journal of Geophysical Research: Planets*,
1082 *110*(E12). https://doi.org/10.1029/2005JE002480

1083 Frost, D. J. (2003). Fe2+-Mg partitioning between garnet, magnesiowustite, and (Mg, Fe) 2SiO4
1084 phases of the transition zone. American Mineralogist, 88(2-3), 387-397.
1085 https://doi.org/10.2138/am-2003-2-315

1086 Frost, D.J., Liebske, C., Langenhorst, F., McCammon, C. a, Tronnes, R.G., Rubie, D.C., 2004.
1087 Experimental evidence for the existence of iron-rich metal in the Earth' s lower mantle. Nature
1088 428, 409–412. https://doi.org/10.1029/200/JC000964

1089 Frost, D.J., McCammon, C.A., 2008. The Redox State of Earth's Mantle. Annu. Rev. Earth
1090 Planet. Sci. 36, 389–420. https://doi.org/10.1146/annurev.earth.36.031207.124322

Frost, D.J., McCammon, C.A., 2009. The effect of oxygen fugacity on the olivine to wadsleyite transformation: Implications for remote sensing of mantle redox state at the 410 km seismic discontinuity. Am. Mineral. 94, 872–882. https://doi.org/10.2138/am.2009.3094

Gaillard, F., & Scaillet, B. (2014). A theoretical framework for volcanic degassing chemistry in a comparative planetology perspective and implications for planetary atmospheres. Earth and Planetary Science Letters, 403, 307-316. https://doi.org/10.1016/j.epsl.2014.07.009

Gaillard, F., Bernadou, F., Roskosz, M., Bouhifd, M. A., Marrocchi, Y., Iacono-Marziano, G., ... & Rogerie, G. (2022). Redox controls during magma ocean degassing. Earth and Planetary Science Letters, 577, 117255. https://doi.org/10.1016/j.epsl.2021.117255

Gao, L., Liu, S, Cawood, P.A., Hu, F., Wang, J., Sun, G., Hu, Y. (2022) Oxidation of Archean upper mantle caused by crustal recycling. Nature Comm. 13, 3283. https://doi.org/10.1038/s41467-022-30886-4

Genda, H., & Ikoma, M. (2008). Origin of the ocean on the Earth: early evolution of water D/H in a hydrogen-rich atmosphere. Icarus, 194(1), 42-52. https://doi.org/10.1016/j.icarus.2007.09.007

Grewal, D. S., Dasgupta, R., Holmes, A. K., Costin, G., Li, Y., & Tsuno, K. (2019). The fate of nitrogen during core-mantle separation on Earth. Geochimica et Cosmochimica Acta, 251, 87-115. https://doi.org/10.1016/j.gca.2019.02.009

Grewal, D. S., Dasgupta, R., & Farnell, A. (2020). The speciation of carbon, nitrogen, and water in magma oceans and its effect on volatile partitioning between major reservoirs of the Solar System rocky bodies. Geochimica et Cosmochimica Acta, 280, 281-301. https://doi.org/10.1016/j.gca.2020.04.023

Hamano, K., Abe, Y. & Genda, H. (2013) Emergence of two types of terrestrial planet on solidification of magma ocean. Nature 497, 607–610. https://doi.org/10.1038/nature12163

Hauri, E. H., Wagner, T. P., & Grove, T. L. (1994). Experimental and natural partitioning of Th, U, Pb and other trace elements between garnet, clinopyroxene and basaltic melts. Chemical Geology, 117(1-4), 149-166. https://doi.org/10.1016/0009-2541(94)90126-0

Herzberg, C., & Zhang, J. (1996). Melting experiments on anhydrous peridotite KLB-1: Compositions of magmas in the upper mantle and transition zone. Journal of Geophysical Research: Solid Earth, 101(B4), 8271-8295. https://doi.org/10.1029/96JB00170

Hier-Majumder, S., & Hirschmann, M. M. (2017). The origin of volatiles in the E arth's mantle. Geochemistry, Geophysics, Geosystems, 18(8), 3078-3092. https://doi.org/10.1002/2017GC006937

1124 Hirose, K. (2002). Phase transitions in pyrolitic mantle around 670-km depth: Implications for
1125 upwelling of plumes from the lower mantle. Journal of Geophysical Research: Solid Earth,
1126 107(B4), ECV-3. https://doi.org/10.1029/2001JB000597

1127 Hirschmann, M.M., 2012. Magma ocean influence on early atmosphere mass and composition.
1128 Earth Planet. Sci. Lett. 341–344, 48–57. https://doi.org/10.1016/j.epsl.2012.06.015

1129 Hirschmann, M. M. (2016). Constraints on the early delivery and fractionation of Earth's major
1130 volatiles from C/H, C/N, and C/S ratios. American Mineralogist, 101(3), 540-553.
1131 https://doi.org/10.2138/am-2016-5452

1132 Hirschmann, M. M. (2021). Iron-wüstite revisited: A revised calibration accounting for variable
1133 stoichiometry and the effects of pressure. Geochimica et Cosmochimica Acta, 313, 74-84.
1134 https://doi.org/10.1016/j.gca.2021.08.039

1135 Hirschmann, M. M. (2022). Magma oceans, iron and chromium redox, and the origin of
1136 comparatively oxidized planetary mantles. Geochimica et Cosmochimica Acta, 328, 221-241.
1137 https://doi.org/10.1016/j.gca.2022.04.005

1138 Hirschmann, M.M. (2023). The deep Earth oxygen cycle: Mass balance considerations on the
1139 origin and evolution of mantle and surface oxidative reservoirs. Earth and Planetary Science
1140 Letters, 619, 118311. https://doi.org/10.1016/j.epsl.2023.118311

1141 Huang, R., Ballaran, T. B., McCammon, C. A., Miyajima, N., Dolejš, D., & Frost, D. J. (2021).
1142 The composition and redox state of bridgmanite in the lower mantle as a function of oxygen
1143 fugacity. Geochimica et Cosmochimica Acta, 303, 110-136.
1144 https://doi.org/10.1016/j.gca.2021.02.036

1145 Irifune, T. (1994). Absence of an aluminous phase in the upper part of the Earth's lower mantle.
1146 Nature, 370(6485), 131-133. https://doi.org/10.1038/370131a0

1147 Jayasuriya, K.D., O'Neill, H.S.C., Berry, A.J., Campbell, S.J., 2004. A Mössbauer study of the
1148 oxidation state of Fe in silicate melts. Am. Mineral. 89, 1597–1609. https://doi.org/10.2138/am-
1149 2004-11-1203

1150 Jennings, E. S., & Holland, T. J. (2015). A simple thermodynamic model for melting of
1151 peridotite in the system NCFMASOCr. Journal of Petrology, 56(5), 869-892.
1152 https://doi.org/10.1093/petrology/egv020

1153 Johnson, K. T. (1998). Experimental determination of partition coefficients for rare earth and
1154 high-field-strength elements between clinopyroxene, garnet, and basaltic melt at high pressures.
1155 Contributions to Mineralogy and Petrology, 133(1-2), 60-68.
1156 https://doi.org/10.1007/s004100050437

1157 Kaminsky, F. V., Ryabchikov, I.D., McCammon, C.A., Longo, M., Abakumov, A.M., Turner, S.,
1158 Heidari, H., 2015. Oxidation potential in the Earth's lower mantle as recorded by ferropericlase

1159 inclusions in diamond. Earth Planet. Sci. Lett. 417, 49–56.
1160 https://doi.org/10.1016/j.epsl.2015.02.029

1161 Kato, T., Ringwood, A. E., & Irifune, T. (1988). Experimental determination of element
1162 partitioning between silicate perovskites, garnets and liquids: constraints on early differentiation
1163 of the mantle. Earth and Planetary Science Letters, 89(1), 123-145. https://doi.org/10.1016/0012-
1164 821X(88)90038-6

1165 Katz, R. F., Spiegelman, M., & Langmuir, C. H. (2003). A new parameterization of hydrous
1166 mantle melting. Geochemistry, Geophysics, Geosystems, 4(9).
1167 https://doi.org/10.1029/2002GC000433

1168 Kite, E. S., & Schaefer, L. (2021). Water on hot rocky exoplanets. The Astrophysical Journal
1169 Letters, 909(2), L22. https://10.3847/2041-8213/abe7dc

1170 Kress, V.C., Carmichael, I.S.E., 1991. The compressibility of silicate liquids containing Fe_2O_3
1171 and the effect of composition, temperature, oxygen fugacity and pressure on their redox states.
1172 Contrib. to Mineral. Petrol. 108, 82–92. https://doi.org/10.1007/BF00307328

1173 Kurnosov, A., Marquardt, H., Frost, D. J., Ballaran, T. B., & Ziberna, L. (2017). Evidence for a
1174 Fe3+-rich pyrolitic lower mantle from (Al, Fe)-bearing bridgmanite elasticity data. Nature,
1175 543(7646), 543-546. https://doi.org/10.1038/nature21390

1176 Kuwahara, H., & Nakada, R. (2023). Partitioning of Fe2+ and Fe3+ between bridgmanite and
1177 silicate melt: Implications for redox evolution of the Earth's mantle. Earth and Planetary Science
1178 Letters, 615, 118197. https://doi.org/10.1016/j.epsl.2023.118197

1179 Kuwahara, H., Nakada, R., Kadoya, S., Yoshino, T., & Irifune, T. (2023). Hadean mantle
1180 oxidation inferred from melting of peridotite under lower-mantle conditions. Nature Geoscience,
1181 1-5. https://doi.org/10.1038/s41561-023-01169-4

1182 Labrosse, S., Hernlund, J. W., & Coltice, N. (2007). A crystallizing dense magma ocean at the
1183 base of the Earth's mantle. Nature, 450(7171), 866-869. https://doi.org/10.1038/nature06355

1184 Lebrun, T., Massol, H., Chassefière, E., Davaille, A., Marcq, E., Sarda, P., Leblanc, F., Brandeis,
1185 G., 2013. Thermal evolution of an early magma ocean in interaction with the atmosphere. J.
1186 Geophys. Res. E Planets 118, 1155–1176. https://doi.org/10.1002/jgre.20068

1187 Liebske, C., Corgne, A., Frost, D. J., Rubie, D. C., & Wood, B. J. (2005). Compositional effects
1188 on element partitioning between Mg-silicate perovskite and silicate melts. Contributions to
1189 Mineralogy and Petrology, 149, 113-128. https://doi.org/10.1007/s00410-004-0641-8

1190 Lin, J. F., Speziale, S., Mao, Z., & Marquardt, H. (2013). Effects of the electronic spin
1191 transitions of iron in lower mantle minerals: Implications for deep mantle geophysics and
1192 geochemistry. Reviews of Geophysics, 51(2), 244-275. https://doi.org/10.1002/rog.20010

1193 Longhi, J., Knittle, E., Holloway, J. R., & Waenke, H. (1992). The bulk composition, mineralogy
1194 and internal structure of Mars. Mars, 184-208. https://doi.org/10.1016/0016-7037(92)90186-M

1195 Luth, R. W., & Canil, D. (1993). Ferric iron in mantle-derived pyroxenes and a new
1196 oxybarometer for the mantle. Contributions to Mineralogy and Petrology, 113(2), 236-248.
1197 https://doi.org/10.1007/BF00283231

1198 Malaspina, N., Langenhorst, F., Fumagalli, P., Tumiati, S., & Poli, S. (2012). Fe3+ distribution
1199 between garnet and pyroxenes in mantle wedge carbonate-bearing garnet peridotites (Sulu,
1200 China) and implications for their oxidation state. Lithos, 146, 11-17.
1201 https://doi.org/10.1016/j.lithos.2012.04.023

1202 Mallmann, G., O'Neill, H.S.C., 2009. The Crystal/Melt Partitioning of V during Mantle Melting
1203 as a Function of Oxygen Fugacity Compared with some other Elements (Al, P, Ca, Sc, Ti, Cr,
1204 Fe, Ga, Y, Zr and Nb). J. Petrol. 50, 1765–1794. https://doi.org/10.1093/petrology/egp053

1205 Mashino, I., Murakami, M., Miyajima, N., & Petitgirard, S. (2020). Experimental evidence for
1206 silica-enriched Earth's lower mantle with ferrous iron dominant bridgmanite. Proceedings of the
1207 National Academy of Sciences, 117(45), 27899-27905. https://doi.org/10.1073/pnas.1917096117

1208 Maurice, M., Tosi, N., Samuel, H., Plesa, A. C., Hüttig, C., & Breuer, D. (2017). Onset of solid-
1209 state mantle convection and mixing during magma ocean solidification. Journal of Geophysical
1210 Research: Planets, 122(3), 577-598. https://doi.org/10.1002/2016JE005250

1211 McCammon, C. A., & Ross, N. L. (2003). Crystal chemistry of ferric iron in (Mg, Fe)(Si, Al) O
1212 3 majorite with implications for the transition zone. Physics and Chemistry of Minerals, 30, 206-
1213 216. https://doi.org/10.1007/s00269-003-0309-3

1214 McCammon, C., Hutchison, M., Harris, J., 1997. Ferric iron content of mineral inclusions in
1215 diamonds from Sao Luiz: A view into the lower mantle. Science (80). 278, 434–436.
1216 https://doi.org/10.1126/science.278.5337.434

1217 McCammon, C.A., Frost, D.J., Smyth, J.R., Laustsen, H.M.S., Kawamoto, T., Ross, N.L., van
1218 Aken, P.A., 2004a. Oxidation state of iron in hydrous mantle phases: Implications for subduction
1219 and mantle oxygen fugacity. Phys. Earth Planet. Inter. 143, 157–169.
1220 https://doi.org/10.1016/j.pepi.2003.08.009

1221 McCammon, C.A., Lauterbach, S., Seifert, F., Langenhorst, F., van Aken, P.A., 2004b. Iron
1222 oxidation state in lower mantle mineral assemblages I. Empirical relations derived from high-
1223 pressure experiments. Earth Planet. Sci. Lett. 222, 435–449.
1224 https://doi.org/10.1016/j.epsl.2004.03.018

1225 McCammon, C.A., Stachel, T., Harris, J.W., 2004c. Iron oxidation state in lower mantle mineral
1226 assemblages II. Inclusions in diamonds from Kankan, Guinea. Earth Planet. Sci. Lett. 222, 423–
1227 434. https://doi.org/10.1016/j.epsl.2004.03.019

McCanta, M. C., Elkins-Tanton, L., & Rutherford, M. J. (2009). Expanding the application of the Eu-oxybarometer to the lherzolitic shergottites and nakhlites: Implications for the oxidation state heterogeneity of the Martian interior. Meteoritics & Planetary Science, 44(5), 725-745. https://doi.org/10.1111/j.1945-5100.2009.tb00765.x

McDonough, W.F., 2003. Compositional Model for the Earth's Core, in: Treatise on Geochemistry. Elsevier, pp. 547–568. https://doi.org/10.1016/B0-08-043751-6/02015-6

Médard, E., & Grove, T. L. (2008). The effect of H_2O on the olivine liquidus of basaltic melts: experiments and thermodynamic models. Contributions to Mineralogy and Petrology, 155, 417-432. https://doi.org/10.1007/s00410-007-0250-4

Mibe, K., Orihashi, Y., Nakai, S. I., & Fujii, T. (2006). Element partitioning between transition-zone minerals and ultramafic melt under hydrous conditions. Geophysical Research Letters, 33(16). https://doi.org/10.1029/2006GL026999

Monteux, J., Andrault, D., Guitreau, M., Samuel, H., & Demouchy, S. (2020). A mushy Earth's mantle for more than 500 Myr after the magma ocean solidification. Geophysical Journal International, 221(2), 1165-1181. https://doi.org/10.1093/gji/ggaa064

Morison, A., Labrosse, S., Deguen, R., & Alboussière, T. (2019). Timescale of overturn in a magma ocean cumulate. Earth and Planetary Science Letters, 516, 25-36. https://doi.org/10.1016/j.epsl.2019.03.037

Moriyama, J., Kawabe, I., Fujino, K., & Ohtani, E. (1992). Experimental study of element partitioning between majorite, olivine, merwinite, diopside and silicate melts at 16 GPa and 2, 000° C. Geochemical Journal, 26(6), 357-382. https://doi.org/10.2343/geochemj.26.357

Miyazaki, Y., & Korenaga, J. (2022). Inefficient water degassing inhibits ocean formation on rocky planets: An insight from self-consistent mantle degassing models. Astrobiology, 22(6), 713-734. https://doi.org/10.1089/ast.2021.0126

Nicklas, R.W., Puchtel, I.S., Ash, R.D., Piccoli, P.M., Hanski, E., Nisbet, E.G., Waterton, P., Pearson, D.G., Anbar, A.D. 2019. Secular mantle oxidation across the Archean-Proterozoic boundary: Evidence from V partitioning in komatiites and picrites. Geochim. Cosmochim. Acta, 250, 49-75. https://doi.org/10.1016/j.gca.2019.01.037

Nimis, P., Goncharov, A., Ionov, D.A., McCammon, C., 2015. Fe^{3+} partitioning systematics between orthopyroxene and garnet in mantle peridotite xenoliths and implications for thermobarometry of oxidized and reduced mantle rocks. Contrib. to Mineral. Petrol. 169. https://doi.org/10.1007/s00410-014-1101-8

Ohtani, E., Kawabe, I., Moriyama, J., & Nagata, Y. (1989). Partitioning of elements between majorite garnet and melt and implications for petrogenesis of komatiite. Contributions to Mineralogy and Petrology, 103, 263-269. https://doi.org/10.1007/BF00402913

O'Neill, H.S.C., Berry, A.J., McCammon, C.C., Jayasuriya, K.D., Campbell, S.J., Foran, G., 2006. An experimental determination of the effect of pressure on the $Fe^{3+}/\sum Fe$ ratio of an anhydrous silicate melt to 3.0 GPa. Am. Mineral. 91, 404–412. https://doi.org/10.2138/am.2005.1929

O'Neill, H.S.C., McCammon, C.A., Canil, D., Rubie, D.C., Ross, C.R., Seifert, F., 1993. Mossbauer spectroscopy of mantle transition zone phases and determination of minimum Fe^{3+} content. Am. Mineral. 78, 456–460.

Otsuka, K., Longo, M., McCammon, C.A., Karato, S. ichiro, 2013. Ferric iron content of ferropericlase as a function of composition, oxygen fugacity, temperature and pressure: Implications for redox conditions during diamond formation in the lower mantle. Earth Planet. Sci. Lett. 365, 7–16. https://doi.org/10.1016/j.epsl.2012.11.030

Pahlevan, K., Schaefer, L., & Hirschmann, M. M. (2019). Hydrogen isotopic evidence for early oxidation of silicate Earth. Earth and Planetary Science Letters, 526, 115770. https://doi.org/10.1016/j.epsl.2019.115770

Pahlevan, K., Schaefer, L., Elkins-Tanton, L. T., Desch, S. J., & Buseck, P. R. (2022). A primordial atmospheric origin of hydrospheric deuterium enrichment on Mars. Earth and Planetary Science Letters, 595, 117772. https://doi.org/10.1016/j.epsl.2022.117772

Pertermann, M., Hirschmann, M. M., Hametner, K., Günther, D., & Schmidt, M. W. (2004). Experimental determination of trace element partitioning between garnet and silica-rich liquid during anhydrous partial melting of MORB-like eclogite. Geochemistry, Geophysics, Geosystems, 5(5). https://doi.org/10.1029/2003GC000638

Pierru, R., Pison, L., Mathieu, A., Gardés, E., Garbarino, G., Mezouar, M., & Andrault, D. (2022). Solidus melting of pyrolite and bridgmanite: Implication for the thermochemical state of the Earth's interior. Earth and Planetary Science Letters, 595, 117770. https://doi.org/10.1016/j.epsl.2022.117770

Purwin, H., Lauterbach, S., Brey, G.P., Woodland, A.B., Kleebe, H.J., 2013. An experimental study of the Fe oxidation states in garnet and clinopyroxene as a function of temperature in the system $CaO\text{-}FeO\text{-}Fe_2O_3\text{-}MgO\text{-}Al_2O_3\text{-}SiO_2$: Implications for garnet-clinopyroxene geothermometry. Contrib. to Mineral. Petrol. 165, 623–639. https://doi.org/10.1007/s00410-012-0827-4

Rohrbach, A., Ballhaus, C., Golla-Schindler, U., Ulmer, P., Kamenetsky, V.S., Kuzmin, D. V., 2007. Metal saturation in the upper mantle. Nature 449, 456–458. https://doi.org/10.1038/nature06183

Rohrbach, A., Ballhaus, C., Ulmer, P., Golla-Schindler, U., & Schönbohm, D. (2011). Experimental evidence for a reduced metal-saturated upper mantle. Journal of Petrology, 52(4), 717-731. https://doi.org/10.1093/petrology/egq101

1299 Rubie, D.C., Frost, D.J., Mann, U., Asahara, Y., Nimmo, F., Tsuno, K., Kegler, P., Holzheid, A.,
1300 Palme, H., 2011. Heterogeneous accretion, composition and core-mantle differentiation of the
1301 Earth. Earth Planet. Sci. Lett. 301, 31–42. https://doi.org/10.1016/j.epsl.2010.11.030

1302 Rubie, D.C., Jacobson, S.A., Morbidelli, A., O'Brien, D.P., Young, E.D., de Vries, J., Nimmo,
1303 F., Palme, H., Frost, D.J., 2015. Accretion and differentiation of the terrestrial planets with
1304 implications for the compositions of early-formed Solar System bodies and accretion of water.
1305 Icarus 248, 89–108. https://doi.org/10.1016/j.icarus.2014.10.015

1306 Rudra, A., Cottrell, E., & Hirschmann, M. M. (2021). Experimental determination of ferric iron
1307 partitioning between pyroxene and melt at 100 kPa. Chemical Geology, 584, 120532.
1308 https://doi.org/10.1016/j.chemgeo.2021.120532

1309 Rudra, A., & Hirschmann, M. M. (2022). Fe^{3+} partitioning between clinopyroxene and silicate
1310 melt at 1–2.5 GPa: Implications for Fe^{3+} content of MORB and OIB source mantle. Geochimica
1311 et Cosmochimica Acta, 328, 258-279. https://doi.org/10.1016/j.gca.2022.04.023

1312 Salters, V. J., Longhi, J. E., & Bizimis, M. (2002). Near mantle solidus trace element partitioning
1313 at pressures up to 3.4 GPa. Geochemistry, Geophysics, Geosystems, 3(7), 1-23.
1314 https://doi.org/10.1029/2001GC000148

1315 Salters, V. J., Longhi, J. E., & Bizimis, M. (2002). Near mantle solidus trace element partitioning
1316 at pressures up to 3.4 GPa. Geochemistry, Geophysics, Geosystems, 3(7), 1-23.
1317 https://doi.org/10.1029/2001GC000148

1318 Schaefer, L. (2023a). Ferric iron evolution in magma ocean models. Stanford Digital Repository.
1319 Available at https://purl.stanford.edu/yg376bh0915 . https://doi.org/10.25740/yg376bh0915 .

1320 Schaefer, L. (2023b). Magma ocean thermal evolution model for determining basal pressure of
1321 last equilibration (bPLE). Stanford Digital Repository. Available at
1322 https://purl.stanford.edu/rk050tc3031 . https://doi.org/10.25740/rk050tc3031 .

1323 Schaefer, L., Wordsworth, R. D., Berta-Thompson, Z., & Sasselov, D. (2016). Predictions of the
1324 atmospheric composition of GJ 1132b. The Astrophysical Journal, 829(2), 63.
1325 https://doi.org/10.3847/0004-637X/829/2/63

1326 Schlichting, H. E., & Young, E. D. (2022). Chemical Equilibrium between Cores, Mantles, and
1327 Atmospheres of Super-Earths and Sub-Neptunes and Implications for Their Compositions,
1328 Interiors, and Evolution. The Planetary Science Journal, 3(5), 127.
1329 https://doi.org/0.3847/PSJ/ac68e6

1330 Shim, S. H., Grocholski, B., Ye, Y., Alp, E. E., Xu, S., Morgan, D., ... & Prakapenka, V. B.
1331 (2017). Stability of ferrous-iron-rich bridgmanite under reducing midmantle conditions.
1332 Proceedings of the National Academy of Sciences, 114(25), 6468-6473.
1333 https://doi.org/10.1073/pnas.1614036114

1334 Solomatov, V. (2007). Magma oceans and primordial mantle differentiation. Evolution of the
1335 Earth, 9, 91-119. https://doi.org/10.1016/B978-044452748-6.00141-3

1336 Solomatov, V. (2015). Magma Oceans and Primordial Mantle Differentiation. Treatise on
1337 Geophysics (Second Edition, ed. G. Schubert, pg. 81-104. https://doi.org/10.1016/B978-0-444-
1338 53802-4.00155-X

1339 Sorbadere, F., Laurenz, V., Frost, D.J., Wenz, M., Rosenthal, A., McCammon, C., Rivard, C.,
1340 2018. The behaviour of ferric iron during partial melting of peridotite. Geochim. Cosmochim.
1341 Acta 239, 235–254. https://doi.org/10.1016/j.gca.2018.07.019

1342 Sossi, P. A., Tollan, P. M., Badro, J., & Bower, D. J. (2023). Solubility of water in peridotite
1343 liquids and the prevalence of steam atmospheres on rocky planets. Earth and Planetary Science
1344 Letters, 601, 117894. https://doi.org/10.1016/j.epsl.2022.117894

1345 Stagno, V., & Aulbach, S. (2021). Redox Processes Before, During, and After Earth's Accretion
1346 Affecting the Deep Carbon Cycle. Magma Redox Geochemistry, 19-32.
1347 https://doi.org/10.1002/9781119473206.ch2

1348 Takahashi, E. (1986). Melting of a dry peridotite KLB-1 up to 14 GPa: Implications on the origin
1349 of peridotitic upper mantle. Journal of Geophysical Research: Solid Earth, 91(B9), 9367-9382.
1350 https://doi.org/10.1029/JB091iB09p09367

1351 Taylor, G. J. (2013). The bulk composition of Mars. Geochemistry, 73(4), 401-420.
1352 https://doi.org/10.1016/j.chemer.2013.09.006

1353 Trail, D., Watson, E.B., Tailby, N.D., 2011. The oxidation state of Hadean magmas and
1354 implications for early Earth's atmosphere. Nature 480, 79–82.
1355 https://doi.org/10.1038/nature10655

1356 Trønnes, R. G. (2000). Melting relations and major element partitioning in an oxidized bulk
1357 Earth model composition at 15–26 GPa. Lithos, 53(3-4), 233-245.
1358 https://doi.org/10.1016/S0024-4937(00)00027-X

1359 Trønnes, R. G., & Frost, D. J. (2002). Peridotite melting and mineral–melt partitioning of major
1360 and minor elements at 22–24.5 GPa. Earth and Planetary Science Letters, 197(1-2), 117-131.
1361 https://doi.org/10.1016/S0012-821X(02)00466-1

1362 Trønnes, R. G., Canil, D., & Wei, K. (1992). Element partitioning between silicate minerals and
1363 coexisting melts at pressures of 1–27 GPa, and implications for mantle evolution. Earth and
1364 Planetary Science Letters, 111(2-4), 241-255. https://doi.org/10.1016/0012-821X(92)90182-U

1365 Van Westrenen, W., Blundy, J. D., & Wood, B. J. (2000). Effect of Fe2+ on garnet–melt trace
1366 element partitioning: experiments in FCMAS and quantification of crystal-chemical controls in
1367 natural systems. Lithos, 53(3-4), 189-201. https://doi.org/10.1016/S0024-4937(00)00024-4

Walter, M. J., Kubo, A., Yoshino, T., Brodholt, J., Koga, K. T., & Ohishi, Y. (2004). Phase relations and equation-of-state of aluminous Mg-silicate perovskite and implications for Earth's lower mantle. Earth and Planetary Science Letters, 222(2), 501-516. https://doi.org/10.1016/j.epsl.2004.03.014

Woodland, A.B., 2009. Ferric iron contents of clinopyroxene from cratonic mantle and partitioning behaviour with garnet. Lithos 112, 1143–1149. https://doi.org/10.1016/j.lithos.2009.04.009

Woodland, A.B., Kornprobst, J., Tabit, A., 2006. Ferric iron in orogenic lherzolite massifs and controls of oxygen fugacity in the upper mantle. Lithos 89, 222–241. https://doi.org/10.1016/j.lithos.2005.12.014

Xie, L., Yoneda, A., Yamazaki, D., Manthilake, G., Higo, Y., Tange, Y., ... & Andrault, D. (2020). Formation of bridgmanite-enriched layer at the top lower-mantle during magma ocean solidification. Nature communications, 11(1), 548. https://doi.org/10.1038/s41467-019-14071-8

Young, E. D., Shahar, A., & Schlichting, H. E. (2023). Earth shaped by primordial H2 atmospheres. Nature, 616(7956), 306-311. https://doi.org/10.1038/s41586-023-05823-0

Yurimoto, H., & Ohtani, E. (1992). Element partitioning between majorite and liquid: a secondary ion mass spectrometric study. Geophysical Research Letters, 19(1), 17-20. https://doi.org/10.1029/91GL02824

Zhang, H.L., Hirschmann, M.M., Cottrell, E., Withers, A.C., 2017. Effect of pressure on $Fe^{3+}/\Sigma Fe$ ratio in a mafic magma and consequences for magma ocean redox gradients. Geochim. Cosmochim. Acta 204, 83–103. https://doi.org/10.1016/j.gca.2017.01.023

Zhang, Z., Dorfman, S. M., Labidi, J., Zhang, S., Li, M., Manga, M., ... & Williams, Q. (2016). Primordial metallic melt in the deep mantle. Geophysical Research Letters, 43(8), 3693-3699. https://doi.org/10.1002/2016GL068560

Table 1. Composition of residual magma ocean liquid following batch crystallization. Starting compositions are the Bulk Silicate Earth (BSE) (McDonough 2003) and Bulk Silicate Mars (BSM) (Taylor 2013). We use lower mantle ferric iron partition coefficients calculated from both the Deng (D) and Armstrong (A) EOSs for the batch calculations.

	Earth					Mars				
Oxide	500 km		1000 km		BSE	500 km		1000 km		BSM
(wt%)	D	A	D	A		D	A	D	A	
FeO	12.7	12.5	11.2	11.0	7.82	24.2	24.2	21.4	21.3	18.1
MgO	31.8	31.2	34.0	33.6	38.3	17.8	17.7	25.2	25.2	31.2
SiO_2	40.1	39.4	42.2	41.7	45.5	49.3	49.3	46.7	46.6	44.6
CaO	10.5	10.3	7.45	7.35	3.58	4.60	4.60	3.27	3.27	2.48
Al_2O_3	4.33	4.25	4.58	4.52	4.49	3.58†	3.57†	3.09†	3.09†	3.15
$FeO_{1.5}$	0.53*	2.42*	0.60*	1.87*	0.36*	0.54**	0.67**	0.41**	0.48**	0.41**
Fe^{3+}/Fe_T	0.037	0.17	0.049	0.15	0.10	0.020	0.025	0.017	0.020	0.02

*reported for initial $Fe^{3+}/Fe_T = 0.10$, **Reported for initial $Fe^{3+}/Fe_T = 0.02$, †assumes $Al_2O_3 = 1.2$wt% in cpx, based on full fractional crystallization model.

1392

1393

Table 2: Parameters for models that switch from batch to fractional crystallization at different depths, including the mass fraction of magma ocean, the pressure and depth at the base of the magma ocean when it transitions from batch to fractional, and the mineral fractions within the solid layer crystallized during the batch step.

	Earth		Mars	
	500 km	1000 km	500 km	1000 km
F_{mo}	0.20	0.39	0.36	0.665
P_{trans} (GPa)	18	37	6.20	12.3
z_{trans} (km)	535	1005	508	1002
T_{trans} (K)	2160	2850	1930	2070
Mineral fractions in batch crystallized layer	Bg 0.90 Mw 0.05 Maj 0.03 Ring 0.02	Bg 0.95 Mw 0.05	Maj 0.15 Ring 0.08 Wad 0.06 Cpx 0.14 Opx 0.07 Gt 0.10 Ol 0.40	Maj 0.31 Ring 0.16 Wad 0.12 Cpx 0.13 Opx 0.03 Gt 0.05 Ol 0.20

1394

1395

Table 3. Ferric iron partition coefficients for the minerals included in our magma ocean model (see also Elkins-Tanton 2008). Partition coefficients for wadsleyite, majorite, ringwoodite, and bridgmanite are calculated using either the Deng or Armstrong (*italic*) EOS for ferric iron in silicate melts (see **Text S2** and **S3** for details). Abbreviations: sp – spinel, ol – olivine, cpx – clinopyroxene, opx – orthopyroxene, gt – garnet, wad – wadsleyite, maj – majorite, ring – ringwoodite, bg – bridgmanite, mw – magnesiowüstite

phase	$D_{Fe^{3+}}^{mineral/melt}$	Ref.
Sp	$exp[(0.87 \pm 0.07)\frac{10{,}000}{T} + (-4.6 \pm 0.4) + (0.24 \pm 0.02) ln\left(C_{Fe_2O_3}^{sp}(wt\%)\right)]$	1
Ol	0	--
Cpx	$\exp\left[(1.997 \pm 0.640) \ln C_{Al_2O_3}^{cpx} + (-3.987 \pm 0.965)\right]$	2
Opx	$(0.70^{+1.56}_{-0.64}) D_{Fe^{3+}}^{cpx/melt}$	3-7
Gt	$(0.68^{+1.95}_{-0.51}) D_{Fe^{3+}}^{cpx/melt}$	3-6
Wad	1.08±0.49 *0.98±0.44*	8
Maj	1.95 ±0.69 *0.97 ±0.34*	8
Ring	2.13±1.17 *0.97±0.53*	8
Bg	2.07±0.50 *0.17±0.03*	9
Mw	0	--

1 – Davis & Cottrell (2021), 2 – refit from Rudra & Hirschmann (2022), 3 - Woodland et al. 2006, 4-Canil & O'Neill 1996, 5 - Malaspina et al. 2012, 6- Nimis et al. 2015, 7-Luth & Canil 1993, 8 – calculated from data in O'Neill et al. 1993, 9 – calculated from data in Boujibar et al. 2016

1396

1397

Table 4. Fit parameters for calculating fO_2 from $\frac{X_{FeO_{1.5}}}{X_{FeO}}$ in silicate melts from equation (12).
Reproduced from Hirschmann (2022), Table 2.

Parameter	Value	Units
a	0.1917	
b	-1.961	
c	4158.1	K
ΔC_p	33.25	J/K
T_0	1673.15	K
y_1	-520.46	K
y_2	-185.37	K
y_3	494.39	K
y_4	1938.34	K
y_5	2888.48	K
y_6	3473.68	K
y_7	-4473.6	K
y_8	-1245.09	K
y_9	-1156.86	K

1398

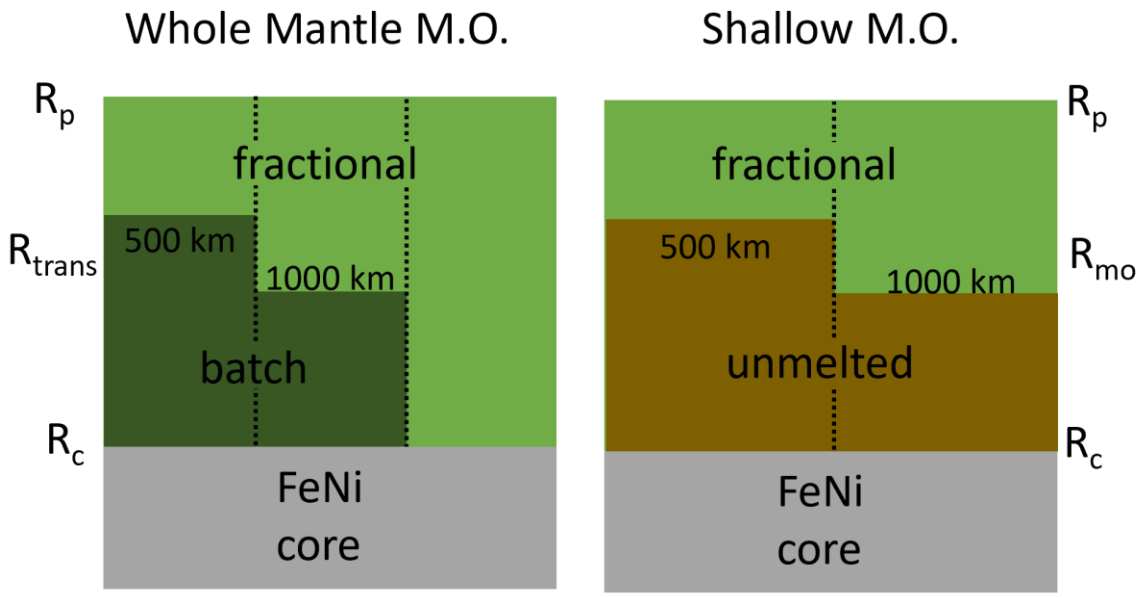

Figure 1. Diagram of model setup showing the differences between the whole mantle models and shallow magma ocean models. All models begin with a BSE or BSM composition (see **Table 1**). In the whole mantle models (*left)*, we assume the magma ocean initially occupies the whole mantle, with either pure fractional crystallization or a mix of batch and fractional crystallization, with the switch occurring once the base of the magma ocean is above R_{trans}. We model batch crystallization as a single stage to find the compositions from which to initialize the fractional crystallization model (see **Table 3**). **Table 2** gives the conditions (P, T, z) at R_{trans}. We adopt the whole mantle magma ocean configurations as our nominal models and show the evolution during the fractional crystallization stages in **Fig. 2** and **Fig. 4**, as well as the solid lines in **Fig. 3** and **Fig. 5**. In the shallow magma ocean models (*right*), we assume that only a portion of the mantle melts ($R_{mo} = R_p - 1000$ km, or $R_p - 500$ km) and solidifies entirely through fractional crystallization. The physical conditions at R_{mo} for the shallow models are the same as for R_{trans} given in **Table 2**. The shallow magma ocean models are shown as dashed lines in **Fig. 3** and **Fig. 5**.

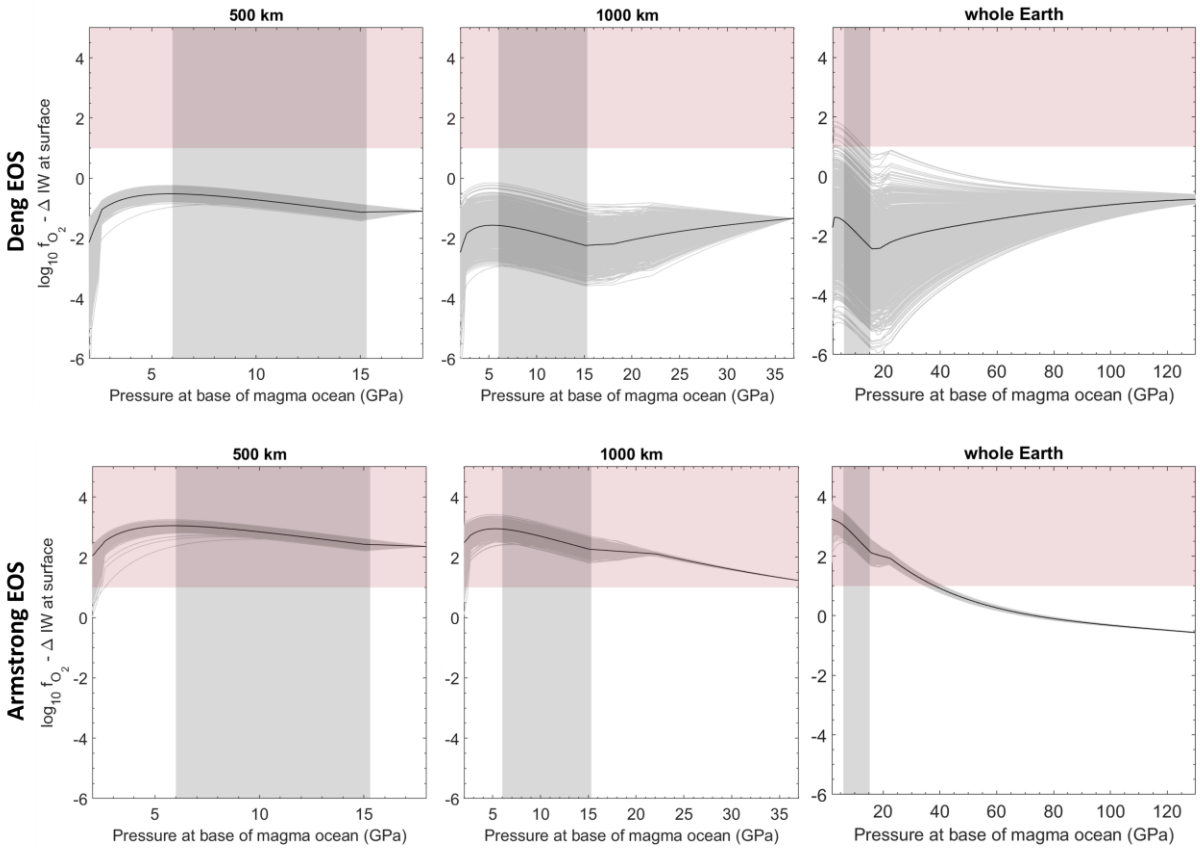

Figure 2. Evolution of oxygen fugacity for the fractional crystallization stages of whole mantle magma ocean models of Earth (see **Fig. 1 (*left*)**). The oxygen fugacity is calculated at the surface of the Earth's magma ocean and is plotted as a function of the pressure at the base of the magma ocean at a given time. Therefore, the x-axis represents time evolution of the magma ocean, with time from the beginning of the magma ocean increasing from right to left. These calculations start with a nominal initial $Fe^{3+}/Fe_T = 0.10$ and use ferric iron partition coefficients calculated from either the Deng EOS (*top row)* or Armstrong EOS (*bottom row*). Oxygen fugacity is shown relative to the iron-wüstite buffer (Hirschmann 2021). The starting conditions for the three models are given in **Table 1**, assuming batch crystallization of the lower mantle for the 500 and 1000 km models. Grey lines are individual simulations with randomly drawn ferric iron partition coefficients, the black line is the average of all 1000 simulations. Pink horizontal shaded region highlights fO_2 permitted by D/H constraint (Pahlevan et al. 2019), vertical grey shaded region highlights basal pressure of last equilibration (BPLEBPLE).

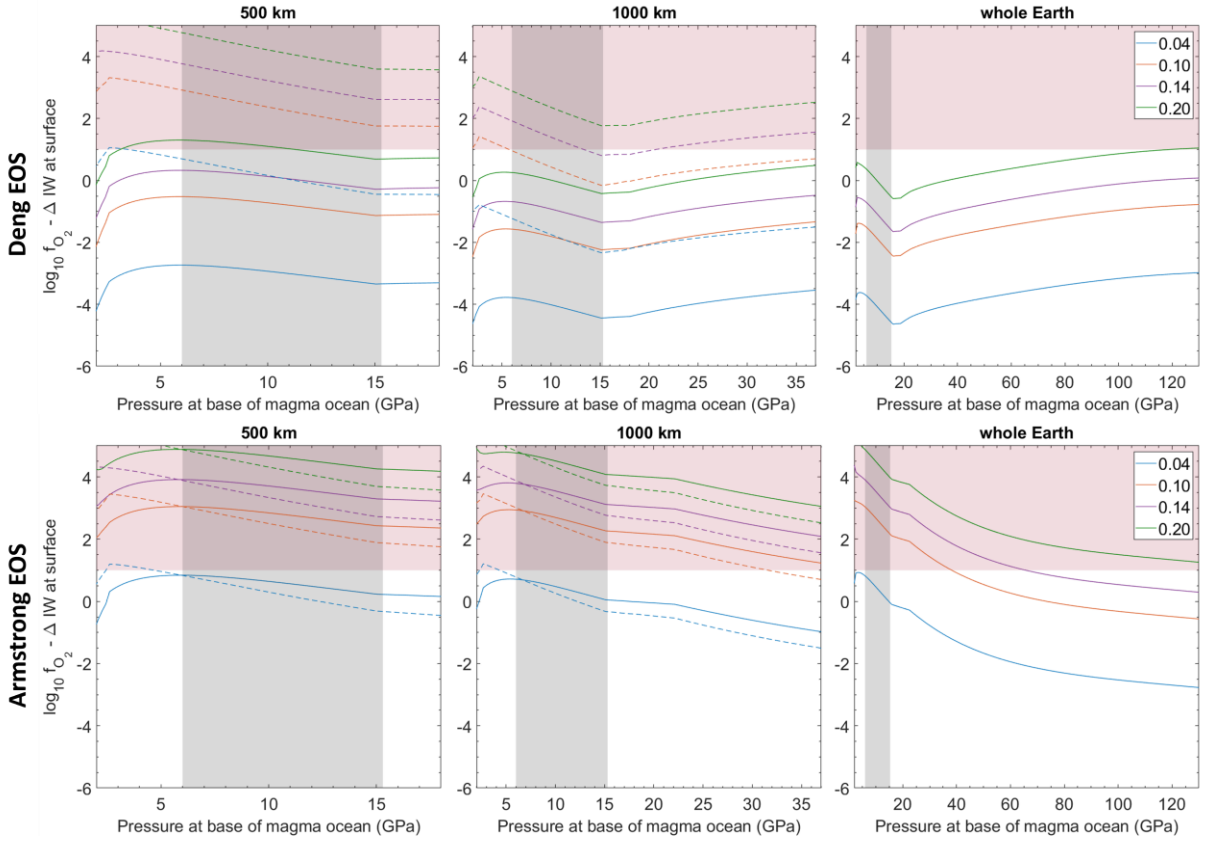

Figure 3. Mean oxygen fugacities at the surface of the Earth's magma ocean for different initial Fe^{3+}/Fe_T (blue: 0.04, red: 0.10, yellow: 0.14, purple: 0.20). The oxygen fugacity is calculated at the surface of the Earth's magma ocean and is plotted as a function of the pressure at the base of the magma ocean at a given time. Therefore, the x-axis represents time evolution of the magma ocean, with time from the beginning of the magma ocean increasing from right to left. Ferric iron partition coefficients were determined with the Deng EOS (*top*) or the Armstrong EOS (*bottom*). All lines represent the mean of 1000 simulations. Solid lines show the fractional crystallization evolution of whole mantle magma ocean models with interstitial liquid = 20% (see **Fig. 1 (*left*)**). Dashed lines are for the shallow magma ocean models (see **Fig. 1 (*right*)**) starting at either 500 km or 1000 km (interstitial = 20%). **Table S5** gives the number of successful simulations for each model configuration. Pink horizontal shaded region highlights fO_2 permitted by D/H constraint (Pahlevan et al. 2019), vertical grey shaded region highlights basal pressure of last equilibration (BPLEBPLE).

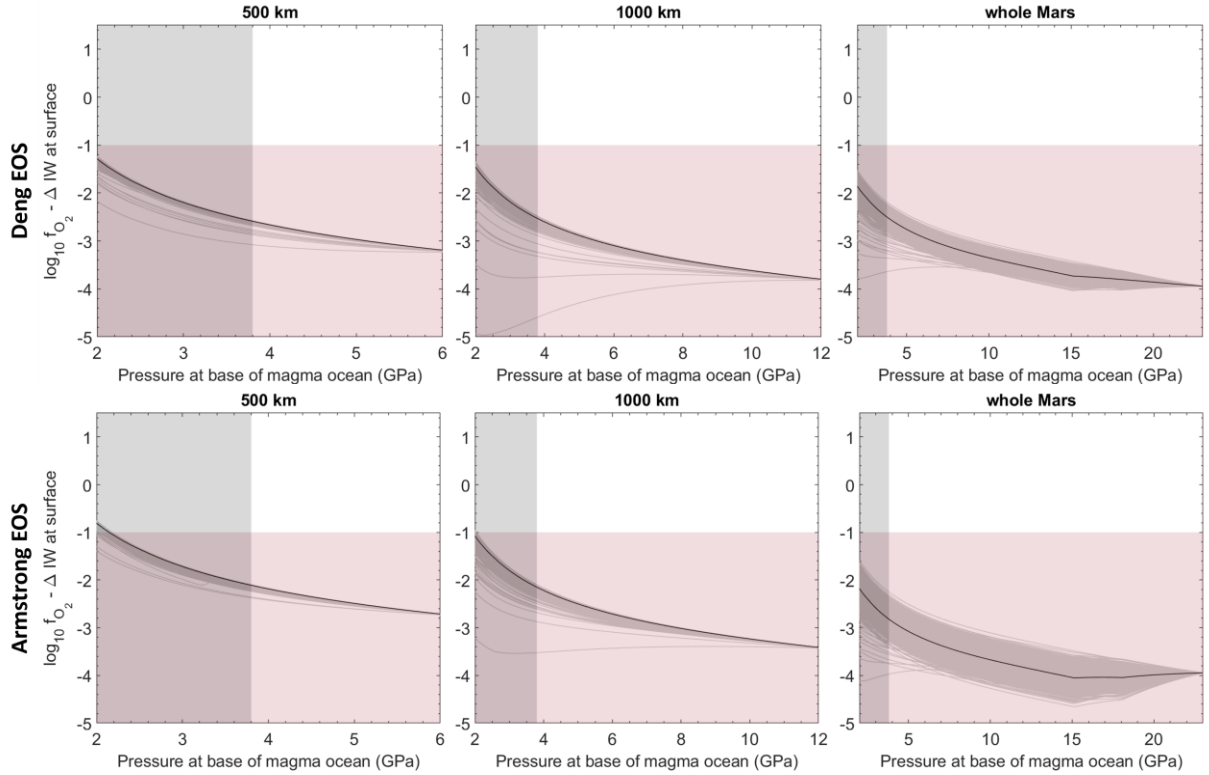

Figure 4. Evolution of oxygen fugacity for the fractional crystallization stages of whole mantle magma ocean models of Mars (see **Fig. 1 (*left*)**). The oxygen fugacity is calculated at the surface of Mars' magma ocean and is plotted as a function of the pressure at the base of the magma ocean at a given time. Therefore, the x-axis represents time evolution of the magma ocean, with time from the beginning of the magma ocean increasing from right to left. These calculations start with a nominal initial $Fe^{3+}/Fe_T = 0.01$ and use ferric iron partition coefficients calculated from either the Deng EOS (*top row*) or Armstrong EOS (*bottom row*). Oxygen fugacity is shown relative to the iron-wüstite buffer (Hirschmann 2021). The starting conditions for the three models are given in **Table 1**, assuming batch crystallization of the lower mantle for the 500 and 1000 km models. Grey lines are individual simulations with randomly drawn ferric iron partition coefficients, the black line is the average of all 1000 simulations. Pink horizontal shaded region highlights fO_2 permitted by D/H constraint (Pahlevan et al. 2022), vertical grey shaded region highlights pressure of last equilibration (BPLEBPLE).

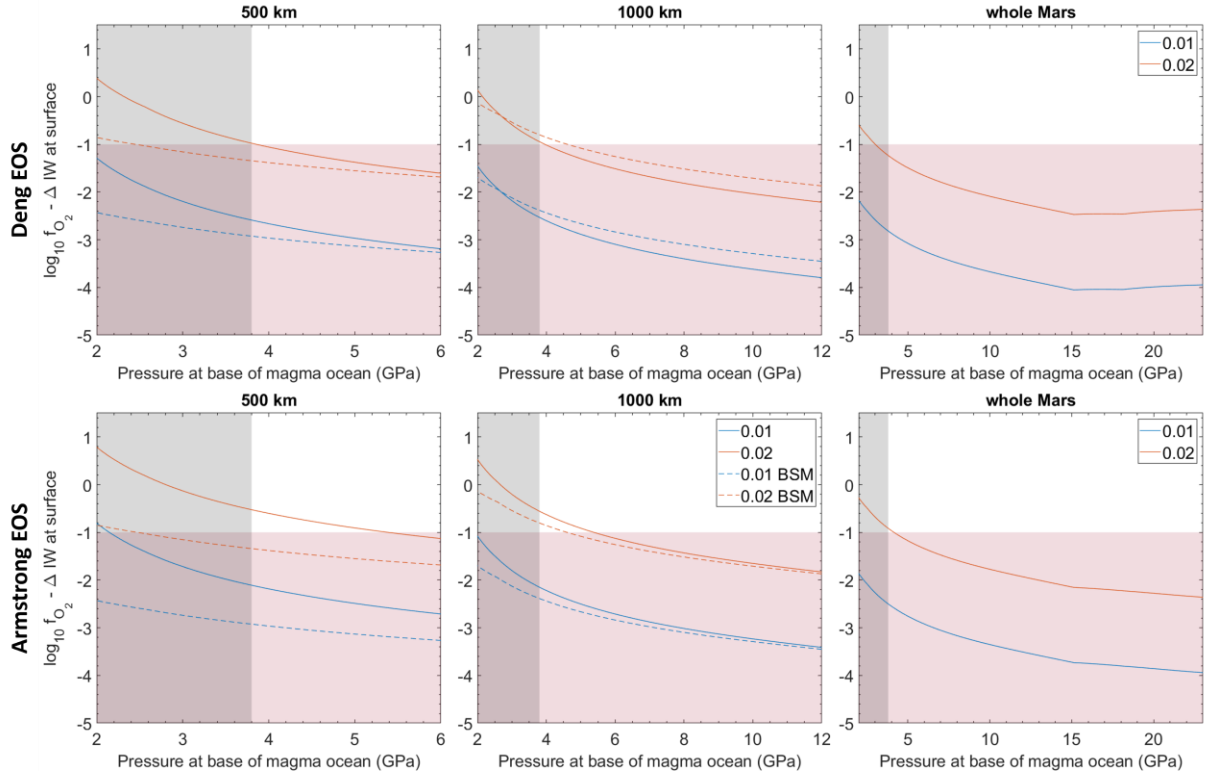

Figure 5. Mean oxygen fugacities at the surface of Mars' magma ocean for different initial Fe^{3+}/Fe_T (blue: 0.01, red: 0.02). The oxygen fugacity is calculated at the surface of Mars' magma ocean and is plotted as a function of the pressure at the base of the magma ocean at a given time. Therefore, the x-axis represents time evolution of the magma ocean, with time from the beginning of the magma ocean increasing from right to left. Ferric iron partition coefficients were determined with the Deng EOS (*top*) or the Armstrong EOS (*bottom*). All lines represent the mean of 1000 simulations. Solid lines show the fractional crystallization evolution of whole mantle magma ocean models with interstitial liquid = 20% (see **Fig. 1 (*left*)**). Dashed lines are for the shallow magma ocean models (see **Fig. 1 (*right*)**) starting at either 500 km or 1000 km (interstitial = 20%). **Table S6** gives the number of successful simulations for each model configuration. Pink horizontal shaded region highlights fO_2 permitted by D/H constraint (Pahlevan et al. 2022), vertical grey shaded region highlights basal pressure of last equilibration (BPLEBPLE).

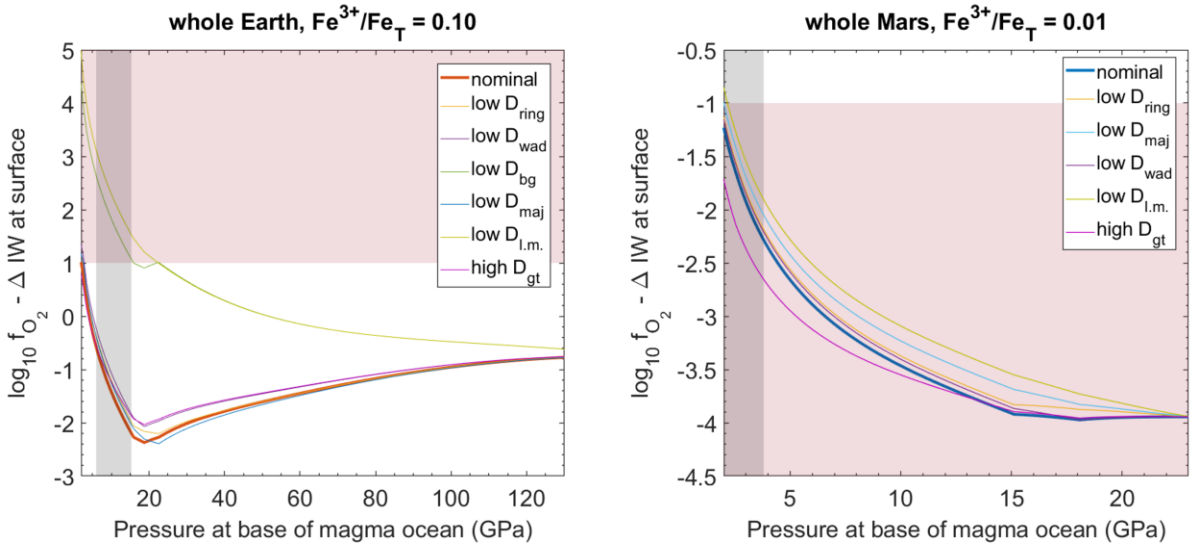

Figure 6. Effect of changing ferric iron partition coefficients of different minerals on the mean oxygen fugacity at the surface of the magma ocean. *Left*: whole Earth magma ocean with $(Fe^{3+}/Fe_T)_{init}$ = 0.10, *right*: whole Mars magma ocean with $(Fe^{3+}/Fe_T)_{init}$ = 0.01. Bold lines show nominal mean values from **Figures 1 & 3**. We reduce the partition coefficients of ringwoodite(18 – 22 GPa), wadsleyite (15-18 GPa), majorite (15 – 22 GPa), bridgmanite (>22 GPa) individually, and all together (l.m. = lower mantle) to 0.5±0.5. We also increase the garnet (2.5 – 15 GPa) partition coefficient to 1.75 ± 0.75.